Atmospheric
Measurement
Techniques

The Pyrenean Platform for Observation of the Atmosphere: site, long-term dataset, and science

Marie Lothon[1], François Gheusi[1], Fabienne Lohou[1], Véronique Pont[1], Serge Soula[1], Corinne Jambert[1], Solène Derrien[1], Yannick Bezombes[1], Emmanuel Leclerc[1], Gilles Athier[1], Antoine Vial[1], Alban Philibert[4,1], Bernard Campistron[1], Frédérique Saïd[1], Jeroen Sonke[2], Julien Amestoy[5], Erwan Bargain[1], Pierre Bosser[6], Damien Boulanger[3], Guillaume Bret[1,✝], Renaud Bodichon[9], Laurent Cabanas[1], Guylaine Canut[7], Jean-Bernard Estrampes[3], Eric Gardrat[1], Zaida Gomez Kuri[1], Jérémy Gueffier[1], Fabienne Guesdon[3], Morgan Lopez[10], Olivier Masson[11], Pierre-Yves Meslin[4], Yves Meyerfeld[1], Nicolas Pascal[8], Eric Pique[1], Michel Ramonet[10], Felix Starck[3], and Romain Vidal[11]

[1]LAERO, Université de Toulouse, CNRS, UT3, IRD, 31400 Toulouse, France
[2]Geosciences Environnement Toulouse, University of Toulouse, CNRS, UPS, 31400 Toulouse, France
[3]Observatoire Midi-Pyrénées, University of Toulouse, UPS, 31400 Toulouse, France
[4]Institut de Recherche en Astrophysique et Planétologie, Université de Toulouse, CNRS, UPS, 31400 Toulouse, France
[5]CEA, DAM, DIF, 91297 Arpajon-Cédex, France
[6]Lab-STICC UMR 6285 CNRS/M3, ENSTA Bretagne/HOP, 29200 Brest, France
[7]CNRM-Université de Toulouse, Météo-France/CNRS, 31100 Toulouse, France
[8]AERIS/ICARE, CNRS/Université de Lille, 59650 Villeneuve d'Ascq, France
[9]ESPRI, Institut Pierre-Simon Laplace (IPSL), 75252 Paris, France
[10]Laboratoire des Sciences du Climat et de l'Environnement (LSCE), IPSL, CEA-CNRS-UVSQ, Université Paris-Saclay, 91190 Gif-sur-Yvette, France
[11]Institut de Radioprotection et de Sûreté Nucléaire (IRSN), PSE-ENV/SERPEN/LEREN, 13115 Saint-Paul-lez-Durance, France
✝deceased, 22 June 2016

Correspondence: Marie Lothon (marie.lothon@aero.obs-mip.fr)

Abstract. The Pyrenean Platform for Observation of the Atmosphere (P2OA) is a coupled plain–mountain instrumented platform in southwestern France. It is composed of two physical sites: the "Pic du Midi" mountaintop observatory (2877 m a.s.l.) and the "Centre de Recherches Atmosphériques" (600 m a.s.l). Both sites are complementarily instrumented for the monitoring of climate-relevant variables and the study of meteorological processes in a mountainous region. The scientific topics covered by P2OA include surface–atmosphere interactions in heterogeneous landscapes and complex terrain, the physics and chemistry of atmospheric trace species at a large scale, the influence of local- and regional-scale emissions and transport on the atmospheric composition, and transient luminous events above thunderstorms.

With a large number of instruments and a high hosting capacity, P2OA contributes to atmospheric sciences through (i) building long-term series of atmospheric observations, (ii) hosting experimental field campaigns and instrumental tests, and (iii) educational training in atmospheric observation techniques.

In this context, P2OA is part of the French component of the Aerosol, Clouds and Trace Gases Research Infrastructure (ACTRIS-Fr) and also contributes to the Integrated Carbon Observation System (ICOS) research infrastructure and to several European or international networks.

Here, we present the complete instrumentation of P2OA and the associated datasets, give a meteorological characterization of the platform, and illustrate the potential of P2OA and its dataset with past or ongoing studies and projects.

1 Introduction

The Pyrenean Platform for Observation of the Atmosphere (P2OA) is a ground-based facility devoted to research in atmospheric sciences. It is composed of two physical sites: the "Pic du Midi" mountaintop observatory (2877 m a.s.l., hereafter PDM) and, 28 km away on the plain, the "Centre de Recherches Atmosphériques" (600 m a.s.l, hereafter CRA).

It is one of the five national multi-instrumented sites of the National Institute of Universe Science (INSU) at the National Centre of Scientific Research (CNRS) devoted to the observation of the atmosphere, and it is one of the foundation stones of the national research infrastructure ACTRIS-Fr, the French component of the Aerosol, Clouds and Trace Gases Research Infrastructure (ACTRIS; Pappalardo et al., 2018). INSU's other instrumented sites for observation of the atmosphere are as follows:

- SIRTA, "Site Instrumental de Recherche par Télédétection Atmosphérique" (Haeffelin et al., 2005), close to Paris;

- CO-PDD, "Cézeaux-Aulnat-Opme-Puy De Dôme" (Baray et al., 2020), in the Auvergne massif, in the centre of France;

- OPAR, "Observatoire de Physique de l'Atmosphère à La Réunion" (Baray et al., 2013), on the island of La Réunion;

- OHP, "Observatoire de Haute Provence", within a Mediterranean forest in southeastern France (see URL in Table B1 in the Appendix).

P2OA thus belongs to a vast variety of ground-based observational platforms settled around the world, which gather, at the same location, a large number of complementary instruments for a comprehensive exploration of atmospheric processes. Ground-based observations are complementary to airborne or spaceborne remote sensing atmospheric measurements since they offer the possibility to operate big, heavy, high-precision, or care-demanding instruments more easily, or over a longer term, than on most mobile platforms. Nowadays, sedentary ground-based atmospheric research stations can be found in almost all geographical environments on Earth:

- polar stations (e.g. Concordia in Antarctica; Argentini et al., 2005);

- maritime stations on isolated islands – often on top of high volcanoes, e.g. Mauna Loa in Hawaii (Keeling et al., 1976), Izaña on the Canary Islands (Gomez-Pelaez et al., 2019), Maïdo on the island of La Réunion (Baray et al., 2013) – or in coastal places (Mace Head in Ireland, Milroy et al., 2012, Cape Grim in Tasmania, Chambers et al., 2016, Barbados Cloud Observatory, Stevens et al., 2016);

- continental stations, as developed below.

There are well-known and widely used sites across the world like the Atmospheric Radiation Measurements (ARM) Southern Great Plains site in the USA (Mather and Voyles, 2013) or Cabauw (Bosveld et al., 2020) in the Netherlands.

ACTRIS (Pappalardo et al., 2018), a European research infrastructure focusing on climate-relevant short-lived atmospheric variables, aggregates no fewer than 79 ground-based observational platforms (https://www.actris.eu/facilities/national-facilities, last access: 14 October 2024), among which the majority are continental stations. Part of these also belong to the dense network of atmospheric stations (around 50) of the Integrated Carbon Observation System (ICOS), the European research infrastructure devoted to greenhouse gas (GHG) monitoring (https://www.icos-cp.eu/observations/atmosphere/stations, last access: 14 October 2024). Continental stations can be roughly categorized into flat-terrain stations vs. mountain stations. Flat-terrain stations are found in either rural (e.g. Cabauw (Bosveld et al., 2020) or Hohenpeissenberg (Leuchner et al., 2015)), peri-urban (SIRTA; Haeffelin et al., 2005), or urban environments (Qualair in Paris; Ammoura et al., 2016), depending on the scientific purposes or operational constraints. Only three sedentary mountain stations can currently be found in the Pyrenean area (Collaud Coen et al., 2018): P2OA is the only one located on the northern side of the chain and that is under oceanic influence; Montsec is a mid-altitude station (1570 m a.s.l.) located about 100 km south–southeast of P2OA, on the Pyrenean southern flank (Pandolfi et al., 2014); and the Montseny station (700 m a.s.l.) is settled on a Mediterranean coastal mountain in the area of Barcelona (Pandolfi et al., 2011). The latter two stations are mainly devoted to aerosol and trace gas observations. P2OA is one of the few platforms which address a broader spectrum of atmospheric issues and observational techniques, with a large number of instruments and a significant hosting capacity being part of its infrastructure. For this, P2OA is involved in ACTRIS, ICOS, and several other international networks devoted to atmospheric surveying.

Despite operational difficulties, mountain sites have long been attractive for scientific experiments of atmospheric sciences (e.g. the proof of atmospheric-pressure vertical gradient by Blaise Pascal at Puy de Dôme in 1648; Baray et al., 2020) or climate monitoring (centennial meteorological data series at, for example, Puy de Dôme and Pic du Midi; Baray

et al., 2020; Marenco et al., 1994). There are several reasons for such attractiveness:

– the mountain meteorology as a research topic in itself

– the need for cold or icing conditions

– far horizontal visibility (e.g. for the optical observation of transient luminous events in the high atmosphere; see Sect. 3.5)

– the thinner atmosphere above (e.g. for the study of cosmic rays interacting with the atmosphere, sun–moon photometer calibration)

– the lesser influence of the continental atmospheric boundary layer and access to free-tropospheric conditions

– situation far from human activity.

Gaining better knowledge of mountain meteorology, especially concerning the small-scale transport processes of atmospheric trace species, is an important challenge. Subgrid-scale vertical transport due to complex topography is not accounted for in global- or regional-scale chemistry transport models (Rotach et al., 2014; Bamberger et al., 2017). This is a major issue since complex topography covers more than 50 % of Earth's continental surface, and small-scale vertical transport may affect, for example, the global carbon balance at the global scale (Rotach et al., 2014) but would certainly also affect other species.

Composed of both a mountaintop station and a lowland station, which are close to each other, with rich instrumentation at CRA to get vertical profiles of the tropospheric dynamics, and atmospheric-composition measurements at both sites, the topographic and instrumental configuration of P2OA is especially suitable for addressing this question, as illustrated in Hulin et al. (2019).

The scientific topics covered by P2OA activity are based on the potential of the two sites in terms of instrumentation, expertise, and geographical embedding:

– atmospheric dynamics, surface–atmosphere interactions, planetary boundary layer over complex terrain and heterogeneous surfaces;

– physics and chemistry of atmospheric trace species at a large scale and their climate impact;

– influence of local- and regional-scale emissions and transport processes on the atmospheric composition;

– atmospheric electricity, especially transient luminous events (TLEs);

– biochemical and geochemical cycles in the environment.

P2OA contributes to atmospheric sciences in three major ways:

– building long-term observation series of climate-relevant variables from a large panel of complementary instruments,

– hosting experimental field campaigns dedicated to atmospheric-process studies or tests of new observation techniques, and

– educational training in the domain of atmospheric observations and instrumental techniques.

The goal of this article is to describe the platform, its instruments, and the associated long-term dataset. It also gives a meteorological characterization of P2OA and reviews past or ongoing scientific studies based on P2OA infrastructure or data in order to illustrate the platform potentials.

2 A plain–mountain double platform in the Pyrenees

P2OA is located on the northern side of the Pyrenees, at a similar distance, as the crow flies, from the Atlantic Ocean to the west (~ 150 km) and from the Mediterranean Sea to the east (~ 200 km). Figure 1 shows the topography of the region and the location of the two sites. The Pyrenees main axis is mostly aligned along the west–east direction (more precisely, along the 300–120° axis). The highest peak is the Pico Aneto, at 3404 m a.s.l., and about 200 summits peak above 3000 m, most of them concentrated in the central part of the massif. On the French side, the main valleys are generally N–S oriented, transversely to the chain axis, while in Spain, the geometry is more complex, with many E–W-aligned sierras and valleys. The terrain lowers much more abruptly on the French side than on the Spanish side.

The CRA site (43.128° N, 0.367° E) is located on the Plateau of Lannemezan, at about 600 m a.s.l., close to the exit of the Aure Valley. The first high ridge to the south, about 15 km away, reaches 1900 m a.s.l. (Bassia Mountain), which is 1300 m above the site. Several small hills and valleys start from the plateau down to the Gers (district) cultivated plain in the north. The Plateau of Lannemezan is covered by grasslands (at ~ 30 %, some of them wetlands or moors) and forests (at ~ 30 %, both deciduous trees and conifers), as well as crops to a lesser degree (mostly wheat and corn). CRA was built in the 1960s by Henri Dessens (1911–1971) for the study of convection and has served atmospheric research since then.

PDM (42.936° N, 0.142° E – about 28 km southwest of CRA), at 2877 m a.s.l., is prominent for its astronomical observatory (Roudier et al., 2021) and its historical meteorological observations, which started in a heroic way in the early 1880s (Dessens and Bücher, 1995). PDM is, nowadays, easily accessible by cable car, with a touristic resort being exploited at the summit. In the scope of P2OA, we consider
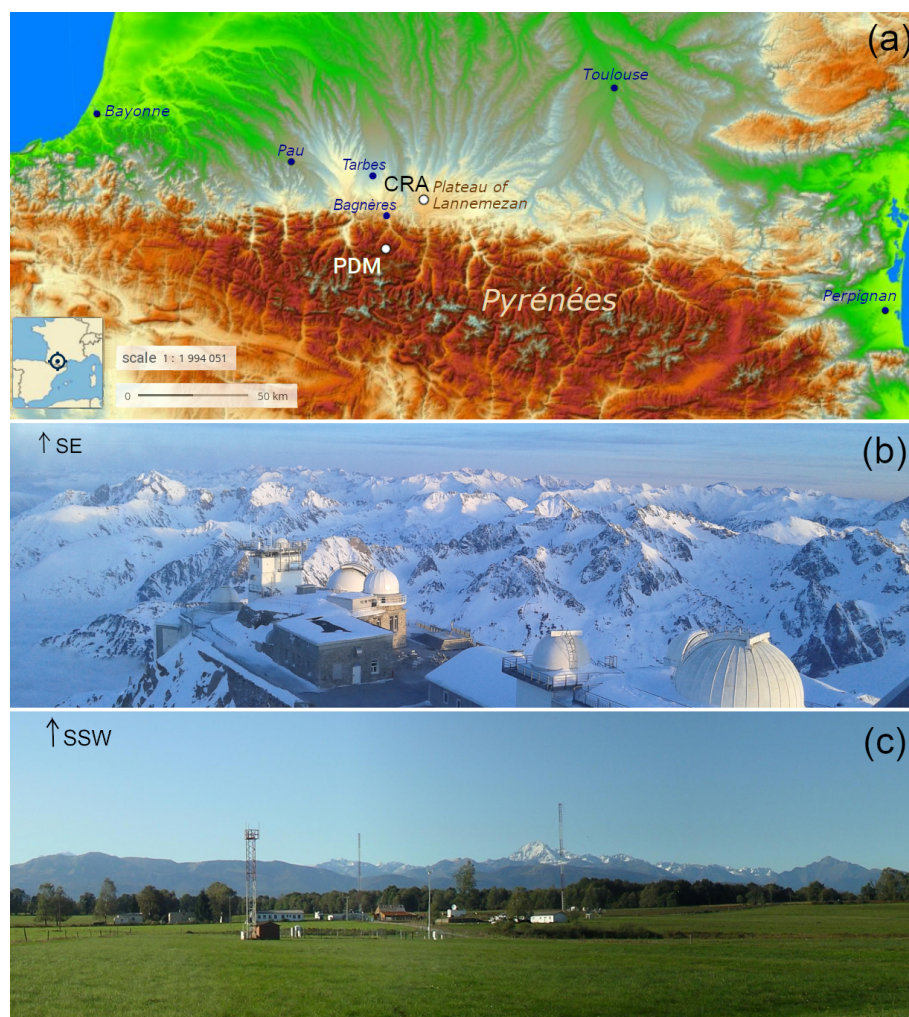
Figure 1. (a) Topography of southwestern France and location of the two P2OA sites, the Pic du Midi (PDM) and the Centre de Recherches Atmosphériques (CRA). © IGN. Main towns are indicated in blue. Green colours from yellow-green to darker green represent altitudes from 0 to 200 m, colours from yellow to red represent altitudes from 200 to 1600 m, colours from red to brown represent altitudes from 1600 to 2300 m, and colours of white and light grey represent altitudes larger than 2300 m. **(b)** Picture of PDM observatory in winter. **(c)** Picture of CRA site. In this picture, PDM is visible, with snow on its top. In panels **(a)** and **(b)**, the sight direction is indicated at the top left of the picture.

only the instrumentation for atmospheric observation, installed on a dedicated platform in the summit buildings. PDM is the only high summit situated 15 km north of the chain of the highest peaks, the latter being concentrated along the French–Spanish border and water divide. This makes PDM a belvedere dominating the French plain and probably justifies its equipment in the 1880s by Charles de Nansouty (1815–1895) and Célestin-Xavier Vaussenat (1831–1891). From a meteorological point of view, it is under the influence of air masses typically coming from the west and is mostly representative of the free-troposphere composition (Sect. 6.1.2). The top of the peak is mostly made of rocks and pastures below.

The populations in radii of 10 and 50 km around PDM amount to about 13 000 and 412 000 inhabitants, respectively, concentrated in two main cities: Pau (217 000 inhabitants) and Tarbes (110 000 inhabitants), situated 55 and 30 km away to the northwest, respectively. A smaller town, Bagnères-de-Bigorre (7000 inhabitants), is located 14 km north of PDM. Lannemezan (6000 inhabitants) is located about 1.5 km east of CRA.

CRA and PDM are both equipped with complementary atmospheric instrumentation, described in the next section. Their infrastructures also allow the hosting of field experiments, education training, and workshops, with lodging and meeting capacity. About eight practical educational training

sessions are hosted every year at P2OA, often organized as dedicated "micro-field campaigns".

3   Instrumentation and data processing

Table 1 shows the list of the instruments in continuous operation at CRA and PDM. The main variables deduced from the measurements are indicated, as well as the algorithms used to obtain them from the raw data and the network to which the instrument is connected. The list of instruments can also be found at https://p2oa.aeris-data.fr/instruments/ (last access: 14 October 2024), along with a description of each instrument. In this section, we present more precisely those instruments and the associated algorithm. The corresponding observational networks are addressed in Sect. 4.

3.1   Meteorological standard variables, surface energy balance, and atmospheric dynamics

Standard meteorological stations from Météo-France have been hosted at the two sites for many years. At PDM, it is actually an exceptionally long historical time series which has been constituted, starting in 1882, maintained alternatively by Météo-France and Observatoire Midi-Pyrénées (the latter being especially helpful during World War II) and bearing witness to the ongoing climate change (Dessens and Bücher, 1995). CRA and PDM stations measure the standard meteorological variables of temperature (2 m), humidity (2 m), pressure, wind (10 m), downward shortwave radiation (2 m), and precipitation at a time interval of 6 min. Another meteorological station is hosted by the InfoClimat French participative science network (Garcelon et al., 2023), with all basic variables measured at 2 m (https://www.infoclimat.fr/observations-meteo/temps-reel/campistrous-centre-de-recherches-atmospheriques/000CE.html#highlight=15, last access: 14 October 2024).

The two sites are equipped with a GNSS antenna as part of the RENAG scientific GNSS network and have been operational since 2011 (RESIF, 2017). The use of GNSS measurements for atmospheric water vapour measurements consists of estimating the propagation delay of GNSS signals in the atmosphere from the raw measurements. The integrated water vapour content can then be extracted from this delay (Bosser and Bock, 2021). The technique is well established and widely used in meteorology and climatology, with an uncertainty of less than $1 \, \mathrm{kg \, m^{-2}}$ (Guerova et al., 2016). The raw GPS data acquired by the two antennas are routinely analysed with a latency of 14 d as part of the ACTRIS-Fr project. Propagation delays are estimated at a rate of 5 min and are converted into integrated water vapour (IWV) using the methodology detailed in Hadad et al. (2018). The method uses hydrostatic delays and mean wet column temperature, which are calculated from 6-hourly ECMWF (European Centre for Medium Range Weather Forecasting) analyses

and are provided by Technische Universität Wien (Boehm et al., 2006).

One of the major instrumented structures of P2OA is the 60 m tower at the CRA site, with five levels of slow meteorological measurements (temperature, humidity, and wind at 0.1 Hz at 2 and 15 m and 1 Hz at 30, 45, and 60 m), and three levels of fast (10 Hz) measurements (temperature, humidity, and wind at 30, 45, and 60 m). The four radiative components are also measured at 60 m with pyranometers (downward and upward shortwave flux) and pyrgeometers (downward and upward longwave flux). All the sensors installed on the 60 m tower are detailed in Table A1. The 60 m tower is mainly surrounded by prairies but with small forests and crops in the vicinity, which more or less also contribute to the footprint, according to the wind and stability. Another flux station is installed at the CRA site at 2 m height within a prairie (fast measurements of temperature, humidity, and wind at 2 m). Contrarily and complementarily to the high tower which integrates a large heterogeneous landscape, this smaller tower measures flux at the scale of a land parcel. Fast measurements with sonic anemometers and hygrometers (LI-COR open-path hygrometers) allow us to calculate the turbulent fluxes and moments, including sensible and latent heat, momentum flux, surface layer stability, and other key turbulence indexes or scales, based on Monin–Obukhov theory. All terms of the surface energy balance between the Earth surface and the atmosphere are thus measured with this instrumentation. The turbulent moments are calculated with the eddy covariance method on 10 and 30 min samples, with the EddyPro® software (Version 6.2.0) from LI-COR Environmental (https://www.licor.com/eddypro, last access: 14 October 2024). The data process options have been discussed within AERIS and ACTRIS-Fr and are homogeneously applied to all ACTRIS-Fr eddy covariance stations.

Complementarily, soil temperature and moisture are measured at six levels in the ground (5, 10, 20, 30, 60, and 120 cm), along with ground flux (5 cm).

Two radar wind profilers complementarily measure the wind vertical profiles from 150 m to 16 km above the ground: a very-high-frequency (VHF) radar and an ultra-high-frequency (UHF) radar. The UHF radar is a Degreane Horizon PCL1300, working at 1274 MHz – that is, 23.5 cm wavelength – with five beams (one vertical beam and four oblique beams at 75° elevation). The sources of echoes are mainly the fluctuations of the air refractive index but also the hydrometeors when it rains and the insects or birds under some conditions. The three components of the wind are deduced every 2 min with a 75 m vertical resolution in a low-acquisition mode or at 150 m resolution in a high-acquisition mode based on the Doppler radial velocities of the five beams, with the velocity and turbulence volume processing technique (Campistron et al., 1991) based on the original velocity azimuth display (VAD) technique (Browning and Wexler, 1968). This radar detects the top inversion of the convective boundary layer (Heo et al., 2003) and also

Table 1. List of permanent instruments at P2OA, with, from left to right, the site where the instrument is located, the type of instrument, the main deduced variables, the start time of the long-term series, the algorithm with which the raw data are processed (if appropriate), the French network or French research infrastructure to which the instrument participates, and the international network or infrastructure. In this table, P, T, and Hu refer to pressure, temperature, and humidity, respectively.

Site	Instrument	Main variable(s)	Start time or period	Process algorithm	FR network or res. infrastr.	Int. network or res. infrastr.
CRA	60 m instrumented tower	P, T, Hu, wind, radiation	2010–		ACTRIS-Fr	
	2 m flux station	Surface energy balance	2010–	EddyPro	Météo-France	
	Meteorological station	Surface energy balance	2014–	EddyPro	StatC	
	Meteorological station	P, T, Hu, wind, rain, radiation	1989–		Météo-France	
	Instrumented pit	P, T, Hu, wind, rain, radiation	2016–		StatC	
	Instrumented pit	Soil temperature and moisture	2019–		ACTRIS-Fr	
	UHF radar wind profiler	Wind, TKE dissipation rate, BL height	2010–	DESMAN	ACTRIS-Fr	E-PROFILE
	VHF radar wind profiler	Wind and tropopause height	2001–	DESMAN	ACTRIS-Fr	E-PROFILE
	Full-sky camera – RAPACE	Cloud cover	2006–	ELIFAN	ACTRIS-Fr	
	Ceilometer CL61	Cloud base height, Z_i, aerosol layers	2022–	STRATFinder	ACTRIS-Fr	TOPROF
	GNSS antenna	Integrated water vapour	2011–		Rénag	
	DOBSON spectrometer	O_3 total column	2004–	O3-DOBSON	ACTRIS-Fr	NDACC
	Reactive gas analysers	O_3, CO, NO_x	2013–		ACTRIS-Fr	
	Greenhouse gas analyser	CH_4, CO, CO_2	2019–		ICOS-Fr	GAW, ICOS
	TLE camera	TLE high-sensitivity images	2007–	UFOCapture		
	Lightning detector	Very-low-frequency radiation	2008–	Time of arrival		Linet
	High-volume sampler	Radionuclide activities	2014–		IRSN Opera	Ro5
	Proportional counter	Gamma eq. dose. rate	2020–		IRSN TELERAY	
PDM	Meteorological station	P, T, Hu, wind	1882–		Météo-France	
	Meteorological station	P, T, Hu, wind, radiation	2004–		ACTRIS-Fr	
	Full-sky camera – EKO	Cloud cover	2017–2019	ELIFAN	ACTRIS-Fr	
	GNSS antenna	IWV	2011–		Rénag	
	Aerosol filter sampling	EC, OC, inorganic ions	2002–		ACTRIS-Fr	ACTRIS-Eu
	Aethalometer	BC mass conc.	2013–		ACTRIS-Fr	ACTRIS-Eu
	Nephelometer	Part. scattering coeff.	2013–		ACTRIS-Fr	ACTRIS-Eu
	Optical particle sizer	Part. size distrib. (0.5–10 μm)	2010–2021		ACTRIS-Fr	ACTRIS-Eu
	SMPS	Part. size distrib. (10 nm–0.8 μm)	2020–		ACTRIS-Fr	ACTRIS-Eu
	Total suspended particle counter	Part. numb. conc.	2013–		ACTRIS-Fr	ACTRIS-Eu
	Reactive gas analysers	O_3, CO	2001–, 2004–		ACTRIS-Fr	GAW, ACTRIS-Eu
	Mercury speciation	GEM, GOM, PBM	2001–			GMOS, iGOS4M
	Flask samples	CO_2, CH_4, CO, N_2O, SF_6	2011–2014		ICOS-Fr	GAW, ICOS
	Greenhouse gas analyser	CH_4, CO, CO_2	2014–		ICOS-Fr	GAW, ICOS
	Radon detector	^{222}Rn volumic activity	2017–		ICOS-Fr	
	High-volume sampler	Radionuclide activities	2018–		IRSN Opera	
	Proportional counter	Gamma eq. dose. rate	2009–		IRSN TELERAY	Ro5
	TLE camera	TLE high-sensitivity images	2009–	UFOCapture		

allows us to estimate the turbulent kinetic energy dissipation rate (Jacoby-Koaly et al., 2002). An improved algorithm for the retrieval of the convective boundary layer (CBL) structure has been developed by Philibert et al. (2024); this can detect thermal internal boundary layers and residual layers in addition to the current CBL growth. Its maximum vertical coverage varies from 1000 m a.g.l. during dry winter days to 9 km during deep convection but always includes the atmospheric boundary layer depth. The minimum height of measurements is close to 150 m a.g.l.

The VHF radar is a partly in-house-developed instrument based on Degreane Horizon and TOMCO systems. It works at 45 MHz – that is, 6.66 m wavelength – with five beams as well (one vertical beam and four oblique beams at 75° elevation). The sources of echoes are almost exclusively the fluctuations of the air refractive index, with parasite echoes from aeroplanes, which are filtered by the process algorithm. The three components of the wind are deduced with the same velocity volume processing technique as for the UHF, with a radial resolution of 375 m and a temporal resolution of 15 min. This radar can measure the wind profile from 1.5 to 16 km a.g.l. It allows us to estimate the tropopause height based on the local maximum of reflectivity generated by the specular echo that occurs at this strong inversion (Campistron et al., 1999; Kim et al., 2001).

The algorithm which produces all the geophysical variables discussed before from the UHF and VHF radar is named DESMAN (Jacoby-Koaly, 2000), and it is related to a GitLab Cecil license, based at the AERIS data centre. It is used for homogeneous processing of several radar wind profilers settled at ACTRIS-Fr sites.

All the instruments described previously are permanent instruments, operating continuously. In addition to this, P2OA is also equipped with mobile meteorological instrumentation, which can be used for educational training and for specific field experiments hosted at the site or elsewhere: a MODEM radiosounding station, a tethered balloon with five meteorological probes, and a flux station.

3.2 Clouds

Both sites are equipped with a total-sky imager, which enables us to visualize the whole sky (2π sr) above each site. They routinely store the full-sky images of the local cloud cover as seen from the ground.

At PDM, the camera is an Eko SRF02 manufactured system operated between 2017 and 2019. At CRA, a homemade system (named RAPACE) is in operation (Lothon et al., 2019), which consists of the association of a digital camera and a large-angle lens (fish-eye). The latter is protected by a plexiglas dome and controlled by a thermostat which keeps the temperature near the lens around 10 °C in order to avoid condensation. RAPACE has been continuously operated at CRA since February 2006, with visible daytime and nighttime images every 15 min (before February 2017) or 5 min

(since then). During the night, a longer 15 s exposure time is used for astronomical applications. The acquisition frequency can be increased anytime (up to 1 Hz) in the context of field experiments or specific demands, with the possibility of making movies.

An algorithm named ELIFAN has been developed (Lothon et al., 2019) in order to estimate the cloud cover from each image. It is based on red / blue ratio thresholding with both an absolute approach and/or a differential approach (with a clear-sky library). All the pixels are thus attributed to categories of cloud, clear sky, or "uncertain". Note that roughly 5 % of the pixels in partly cloudy images are attributed to the uncertain category, which gives an estimation of ELIFAN uncertainty. ELIFAN has been generalized and adapted to several other sky cameras like the Eko camera of the Pic du Midi and other total-sky cameras of the ACTRIS-Fr infrastructure. It is associated with a GitLab Cecil license.

Cloud base height is estimated from a ceilometer. From 2016 to 2019, a ceilometer Vaisala 25K was present at the CRA site, giving estimates of cloud base height at three potential levels. Starting in April 2022, a new Vaisala CL61 ceilometer was installed, with improved capabilities: it can detect cloud base up to 16 km above ground, give information on the vertical distribution of aerosols derived from the backscatter profiles, and also measure the linear depolarization ratio. The latter enables us to distinguish spherical particles from dissymmetrical particles, like liquid water from ice within clouds or precipitation, and types of aerosols. This ceilometer also enables us to estimate the boundary layer top. Through participation in E-PROFILE, the STRATFinder (Kotthaus et al., 2020) algorithm will be applied in the future; this supplies different interfaces from the vertical structure, including the convective boundary layer top.

The knowledge of cloud occurrence at the PDM summit – that is, whether it is immersed within cloud or not – is relevant for in situ measurements of soluble-gas concentrations or aerosol properties. Since April 2022, a binary index indicating cloudy conditions at PDM (called the in-cloud index) has been derived from images taken every 5 min with a webcam showing details of the summit platform (from a few metres to 150 m away from the camera), as well as the background mountain landscape. A similar approach was developed by Baray et al., 2019 for the Puy de Dôme observation platform. The algorithm is based on edge detection using a Canny filter on several areas in the image, selected at various distances. Areas with sharp contours are considered to be free of cloud, while blurred contours are considered to be the signature of fog between the scene and the camera. These various pieces of information are then merged using a fuzzy-logic algorithm, finally returning 0 (false) as the value for clear air or 1 (true) for the presence of cloud.

3.3 Atmospheric trace gases

3.3.1 Reactive gases

O_3 and CO

In the decades following Schönbein's discovery of ozone (O_3) in 1839 and the characterization of the molecule (trioxygen) by Soret in 1865, the question regarding the presence of this gas in the atmosphere arose. Among the very first historical tropospheric-ozone measurements, some were conducted at the Sencours station – settled at a saddle point 500 m below the PDM summit – as early as in 1874 and then at the new summit station from 1881 to 1909 using the Schönbein method (Marenco et al., 1994). Modern measurement series by UV absorption analysers were conducted at PDM in 1982 (Marenco, 1986), in 1990–1993 (Marenco et al., 1994), and then continuously from 2001 to present. Compilation of all those data series revealed an increase in tropospheric ozone by a factor 5 from the 1900s to the early 1990s (Marenco et al., 1994) but a stabilization around 45 nmol mol^{-1} since then (Chevalier et al., 2007). As a chemical precursor of tropospheric ozone, carbon monoxide (CO) was also measured during the 1982 campaign (Marenco, 1986) and continuously since 2004 by trace-level IR absorption analysers (Gheusi et al., 2011). Technical details on the O_3 and CO instruments, as well as uncertainty calculations, are given in Gheusi et al. (2011). The World Meteorological Organization (WMO) Global Atmospheric Watch (GAW) standard operation procedures (GAW, 2013, 2010, for O_3 and CO, respectively) are followed at PDM.

The stratospheric ozone is also monitored at P2OA, with a Dobson UV spectrometer which measures the total ozone column by means of the O3EDOBSON (http://www.o3soft.eu/, last access: 14 October 2024) algorithm.

Mercury

In May 2011, automated atmospheric-mercury speciation sensors were installed at PDM for gaseous elemental mercury, gaseous oxidized mercury, and particulate-bound mercury. The instrumentation was operated until the end of 2014 by the Geosciences Environnement Toulouse research institute and was composed of a Tekran ambient mercury vapour analyser (model 2537A/B), a mercury speciation unit (model 1130), and a particulate mercury unit (model 1135). PDM joined the Global Mercury Observation System (GMOS; see Table B1) project as an external site in 2012.

3.3.2 Greenhouse gases

Continuous measurements of the two main greenhouse gases, carbon dioxide (CO_2) and methane (CH_4), as well as of carbon monoxide (ancillary of CH_4 measurements), have been conducted in the framework of the national RAMCES/ICOS network since May 2014 at PDM (https://icos-atc.lsce.ipsl.fr/panelboard/PDM, last access: 14 October 2024) and since April 2019 at CRA (https://icos-atc.lsce.ipsl.fr/panelboard/CRA, last access: 14 October 2024). These measurements are made at both sites by means of Picarro G24 analysers based on cavity ring-down spectroscopy (Yver-Kwok et al., 2015). The applied QA/QC protocol (traceability of data and calibration chain, regular human-eye data check, etc.) is defined by the European programme ICOS.

Prior to these continuous greenhouse gas measurements, air flask sampling was made weekly from 2002 at PDM. Flasks were then sent to the RAMCES service at LSCE for laboratory analyses of CO_2 (with speciation of isotopes ^{13}C and ^{18}O), CH_4, CO, N_2O, and SF_6.

3.3.3 Radon and radioactivity

Radon is an inert radioactive gas emitted from ice-free soils with a half-life of 3.8 d, making it a useful tracer of the atmospheric boundary layer dynamics and thus a reliable tracer to discriminate between air masses recently influenced by the continental boundary layer and the free troposphere (Chambers et al., 2013). A highly sensitive radon monitor manufactured by the Australian Nuclear Science and Technology Organisation (model 1500L; Whittlestone and Zahorowski, 1998) has been in operation at PDM since October 2017.

Continuous monitoring of radon concentrations has also been performed at three different heights of the CRA 60 m tower (at 1, 30, and 60 m) with AlphaGUARD ionization chambers since 2018 (Amestoy, 2021). Atmospheric radon is also monitored by gamma-ray spectroscopy using a RSX-5 NaI spectrometer mounted on the same tower, and soil concentrations of radon are measured by means of three BARASOL probes (Amestoy et al., 2021).

P2OA hosts 2 of the 50 national aerosol samplers for the monitoring of atmospheric radioactivity as part of the Permanent Observatory of Atmospheric Radioactivity (IRSN OPERA) network. A very-high-flow-rate sampler ($900 m^3 h^{-1}$, before temperature and pressure corrections) is equipped at PDM, making it the most sensitive altitude station in terms of trace-level radionuclide measurements. At both P2OA sites, samples are taken on a weekly basis. Both samplers make it possible to detect naturally occurring radionuclides, such as cosmogenic ones (e.g. ^7Be, ^{22}Na), as well as any long-lived artificial radionuclides (e.g. ^{137}Cs) resulting from past nuclear tests or shorter-lived ones which could indicate a nuclear-accident release. Results can be downloaded at https://www.mesure-radioactivite.fr/#/ (last access: 14 October 2024). These devices closely complement the high-frequency measurements of automatic alert probes (TELERAY network) which would react instantly in the event of high contamination.

3.4 Physical, chemical, and optical properties of aerosols

At PDM, the chemical composition of aerosols has been measured since 2002. Weekly filter samples are taken from a pumped volume of air of approximately $400\,m^3$. They are then analysed to provide the concentrations of elemental carbon (EC) and organic carbon (OC) through a thermo-optical analytical technique (EUSAAR protocol; Cavalli et al., 2010) on the one hand and the concentrations of major inorganic ions (calcium, magnesium, sulfate, nitrate, potassium, chlorine, ammonium) through analysis by ion chromatography on the other hand.

Aerosol optical properties have been measured since 2013. Scattering measurements were implemented for one wavelength from 2013 to 2018 (Nephelometer Ecotech M9003) and then for three wavelengths from 2018 to present (Nephelometer Ecotech AURORA 3000). Aerosol absorption properties were measured first (2013–2017) for one wavelength and then for seven wavelengths (2017–present) with a Magee AE16 and then with an AE33 Aethalometer, respectively.

The total aerosol number concentration was measured from 2008 by a condensation particle counter (TSI CPC 3010) until 2020 and then by a CPC 3750 thereafter.

Finally, the aerosol size distribution measurement was initially performed only in the coarse mode (0.5–10 µm) from 2010 to 2021 thanks to the implementation of an optical particle sizer (TSI OPS 3330), and then, from 2020, the aerosol size distribution from 10 nm to 0.8 µm was performed by the implementation of a size mobility particle spectrometer (model 4S from Paolo Vilani société 4S).

3.5 Transient-luminous-event optical observations

Two low-light WATEC 902H cameras (minimum illumination of 10^{-4} lx) are installed at the two P2OA sites. They have a field of view of 31° and are oriented toward the storm with a pan-tilt unit that can be remotely controlled via the internet. Thus, the observations of transient luminous events (TLEs) can be made under nighttime conditions above thunderstorms in a range of about 800 km around each site at the altitudes of these phenomena (between 30 and 90 km) and on alert according to the meteorological conditions. The cameras operate in a triggered mode provided by the UFO-CaptureV2 software (https://sonotaco.com/soft/e_index.html (last access: 14 October 2024) to capture luminous events with brightness above a given threshold. They provide videos with a time resolution of 25 frames (or 50 interlaced fields) per second, which corresponds to a time resolution of 20 ms. The azimuth and elevation of the sprite events are determined with the software "Cartes du Ciel" (SkyChart). The methodology for the analysis of the video imagery; the time and space synchronization with other data regarding the storm activity, especially the lightning flashes associated with the

TLEs; and the event terminology are explained in Soula et al. (2017).

4 Data dissemination

4.1 Infrastructures and networks

Most of the permanent instruments at P2OA participate in national or international atmospheric monitoring networks. These are indicated in Table 1 in relation to each instrument. All networks or infrastructures pursue common objectives: sharing expertise on improving data quality and standardizing the observing systems, procedures, data bases, data processing, and data dissemination. They also favour the research and development, educational training, technical assistance, and production of essential output information in relation to end-users.

4.1.1 ACTRIS

P2OA is intrinsically linked with the national ACTRIS-France infrastructure (hereafter ACTRIS-Fr), the French component of the European ACTRIS infrastructure (Pappalardo et al., 2018). ACTRIS is a distributed infrastructure in support of research on climate and air quality for a better understanding of the evolution of processes and atmospheric composition. It supplies information on the variability of climate-relevant reactive species from multiple observational and exploration platforms. ACTRIS-Fr has a larger scope than ACTRIS-ERIC (European Research Infrastructure Consortium, also ACTRIS-Eu in Table 1) due to also including fundamental variables of climate and meteorology, namely atmospheric dynamics and surface–atmosphere heat fluxes. The plain involvement of P2OA within ACTRIS-Fr explains why so many instruments participate in this infrastructure (see Table 1). Only aerosols and trace gas continuous monitoring conducted at PDM have participated to date within the European scale of the infrastructure, with involvement in two of the six ACTRIS topical centres: the European Centre for Aerosol Calibration and Characterization and the Centre for Reactive Trace Gases In Situ Measurements.

By construction, ACTRIS-Fr is thus a convergence point for many networks, which is beneficial: the infrastructure helps the involved sites in maintaining their instrumentation and monitoring, in the data dissemination, in bringing about national scientific research dynamics, etc., while the network brings about specific scientific questions, dynamics, and tools relevant to the European or international community.

4.1.2 ICOS-ATC

Greenhouse gases measured at both PDM and CRA participate in the Integrated Carbon Observation System – Atmospheric Thematic Centre (ICOS-ATC) at the European scale

(Heiskanen et al., 2022). ICOS produces standardized long-term observations to understand the carbon cycle and to monitor greenhouse gases for a better understanding of climate change and its impacts. Atmospheric measurements of CO_2 and CH_4 at both PDM and CRA contribute to the European Obspack compilation updated once a year. The data are available on the ICOS Carbon portal (Bergamaschi et al., 2024a, b for respectively CO_2 and CH_4).

4.1.3   Météo-France

The two meteorological stations of P2OA managed by Météo-France – the French national meteorological service – are part of its synoptic network, providing operational observation data for assimilation by the numerical weather prediction (NWP) models ARPEGE and AROME and for climate monitoring.

4.1.4   E-PROFILE

The two wind profilers and the ceilometer participate in E-PROFILE, a programme of the European Meteorological Network, EUMETNET (see Table B1). E-PROFILE is part of the EUMETNET Composite Observing System, managing the European networks of radar wind profilers, lidars, and ceilometers for the monitoring of vertical profiles of wind and aerosols. Near-real-time data of the two P2OA wind profilers are sent every 30 min to the network, with constraints of timeliness for the global forecast system to assimilate the data on time. Monthly statistical monitoring of the model–observation departure is supplied by the network and by Météo-France.

4.1.5   GAW

The Global Atmosphere Watch (GAW) programme (see Table B1) of the World Meteorological Organization (WMO) aims to improve the global understanding of atmospheric composition and coordinates the collection of high-quality atmospheric-composition observations from stations all over the world. Owing to the remote character of the site and the panel of long-term observations conducted there, PDM has been accepted as a GAW regional station since 2018.

Beforehand, PDM had already contributed to GAW databases for many years:

- to the World Data Centre for Greenhouse Gases (see Table B1), hosted by the Japan Meteorological Agency since 2001;

- to the World Ozone and Ultraviolet Radiation Data Centre (see Table B1), hosted by the Canadian government since 2004 (see the NDACC section below);

- to the World Data Centre for Reactive Gases, hosted at the Norwegian Institute for Air Research on the

so-called "EBAS" system (see Table B1) since 2007 (ozone);

- to the World Data Centre for Aerosols since 2013.

4.1.6   NDACC

The Network for the Detection of Atmospheric Composition Change (NDACC; see Table B1) is an international collaboration and a worldwide network of ground-based stations for remote sensing observations of (mainly) water vapour and ozone in the whole atmosphere (from the troposphere to the mesosphere). At the national scale, observations are coordinated by the NDACC-France service. P2OA contributes to the NDACC database (and, at the same time, to the GAW World Ozone and Ultraviolet Radiation Data Centre) with data from a Dobson UV spectrometer (historical instrument no. 49) that has operated at CRA since 2004.

4.2   Data and physical-access policies

4.2.1   Data policy

The data are available from the P2OA web portal (https://p2oa.aeris-data.fr/data/, last access: 14 October 2024) but are also accessible from the ACTRIS-Fr web portal (https://www.actris.fr/, last access: 14 October 2024) and the AERIS data catalogue (https://www.aeris-data.fr/en/catalogue-en/, last access: 14 October 2024) for the concerned variables, with no differences between the datasets according to the portal used. Long-term observation data collected on any P2OA site are ruled by the P2OA data policy, which is available here: https://p2oa.aeris-data.fr/p2oa-data-policy/ (last access: 16 October 2024). The data policy follows the ACTRIS-Fr data policy for any variable lying in the contour of ACTRIS-Fr.

The main spirit of P2OA and ACTRIS-Fr data policies is to offer free and unlimited access to P2OA data.

The users agree to contact the concerned local principal investigators to offer an appropriate level of acknowledgement or collaboration. In all cases, publications using P2OA long-term observation data should include the acknowledgement formula proposed in the data policy (or an appropriate adaptation of it).

4.2.2   Site physical access – hosting policy

Observation data collected on P2OA sites in the context of temporary campaigns are not the concern of the data policy but rather of the P2OA hosting policy available at this address: https://p2oa.aeris-data.fr/physical-access-form/ (last access: 16 October 2024).

Beyond this policy, the temporary users of P2OA experimental sites are invited to fill in a physical access form, where the technical needs of their experiment should be described in sufficient detail, beforehand. Required at least 1 month in

advance, this form allows P2OA staff to assess the feasibility of the project and to prepare the best technical conditions for the experiment in close collaboration with the hosted research team.

Again, the users are requested to agree with the local principal investigators on the appropriate level of collaboration. As a minimum requirement, the acknowledgement formula mentioning P2OA should appear in any publication.

4.3 The ReOBS project

For facilitated access to the multi-instrumental data collected at observatories, the ReOBS project (see Table B1) (Chiriaco et al., 2018) aims to gather and synchronize multiple datasets from a given observatory in one single NetCDF file at a 1 h time resolution. Chiriaco et al. (2018) more specifically deal with the data of the SIRTA observatory (Instrumented Site for Remote Sensing Atmospheric Research), from which the project started. Since then, in the context of ACTRIS-Fr and its aim to harmonize the data and their access from the national AERIS data centre, the ReOBS project has been extended to other observatories, with P2OA among them. This is part of ongoing work at P2OA to make a single file of a large set of relevant data at 1 h time resolution for easier use by external users like modellers, air quality services, etc. ReOBS also merges native-resolution data for principal investigators or more specific uses. It includes an additional data quality-controlling procedure and statistics.

5 Meteorological characterization of P2OA area

Here, we present a meteorological characterization of P2OA based on the meteorological measurements performed over a 8-year period at P2OA, from 2015 to 2022. A flow regime study has previously been carried out by Gueffier (2023) over the period 2015–2019 based on hierarchical ascendant classification, which gives support to our discussions below. In Sect. 5.4, we used the same dataset (and same period) as Gueffier (2023) for the benefit of good data coverage for all variables, synchronization at a common hourly time base, and careful data quality control. Starting in 2015 enables us to work with the most homogeneous dataset (there are UHF data from 2010 to 2015 which still need to be processed in a homogeneous way). We first address the flow regimes based on the radar wind profiler data and the 60 m tower data. Then we illustrate the seasonal variability of thermodynamic variables, radiation, cloud cover, precipitation, and convective boundary layer depth. Third, we present the long-term temperature trend. We end this section with the seasonal and diurnal variability of the atmospheric composition observed at PDM.

5.1 Flow regimes

The meteorological conditions observed at P2OA are governed by the presence of the Pyrenees chain. Dynamically, and at the regional scale, we observe the following:

- the typical westerly or northwesterly synoptic winds are channelled along the chain;

- northerlies, often associated with anticyclonic conditions, can be blocked by the chain on the French side;

- southerly or southwesterly winds, often associated with a low located over the Atlantic, lead to mountain waves, flow splitting, and foehn situations;

- easterlies, although rare, are also channelled along the chain, and they are sometimes linked with a low situated over the Mediterranean Sea and with enhanced precipitation over the eastern part of the Pyrenees.

Figure 2 presents the wind roses found over the period 2015–2022 at three different altitude levels in the lower troposphere based on three different instruments operated at CRA (the VHF and UHF wind profilers and the 60 m tower). The highest level shown, at 4000 m a.s.l., shows the predominance of synoptic winds in a large southwest-to-northwest quadrant. At 750 m a.g.l., the wind rose looks totally different and shows the channelling of the flow along the chain. Close to the surface (15 m above the ground), a superposition of different flow regimes is visible: in addition to the dominant westerlies, thermally induced winds are frequent, characterized by southerly drainage (katabatic) flow from the mountain during the night and a northerly up-mountain (anabatic) breeze during the day (Hulin et al., 2019). Note that the surface wind at CRA is generally weak, except in cases of rare strong westerly fronts or southerly downslope wind storms. The area, centrally close to the foothills of the Pyrenees and protected by them, is one of the areas in France with the weakest winds.

The plain–mountain thermal wind is connected to the valley winds of the Aure Valley mentioned before. It usually sets up in calm synoptic conditions but can still be established under significant synoptic forcing, especially when the northern Pyrenean foreland is sheltered by the mountains from southerly to southwesterly wind blowing at altitude. Hulin et al. (2019), based on the 2006–2015 dataset, found that almost 30 % of days with surface breeze at CRA occur under conditions with a southerly wind component of more than 5 m s^{-1} aloft. They also found an overall occurrence of 27.5 % for days with a surface breeze at CRA. Román-Cascón et al. (2019) have shown that, for the year of 2017, the katabatic winds at CRA lay in the sector of 110–200° and had a large occurrence, more than 30 % of time. Anabatic winds are less frequent – about 15 % of the time – and lie in the sector of 300–50°.
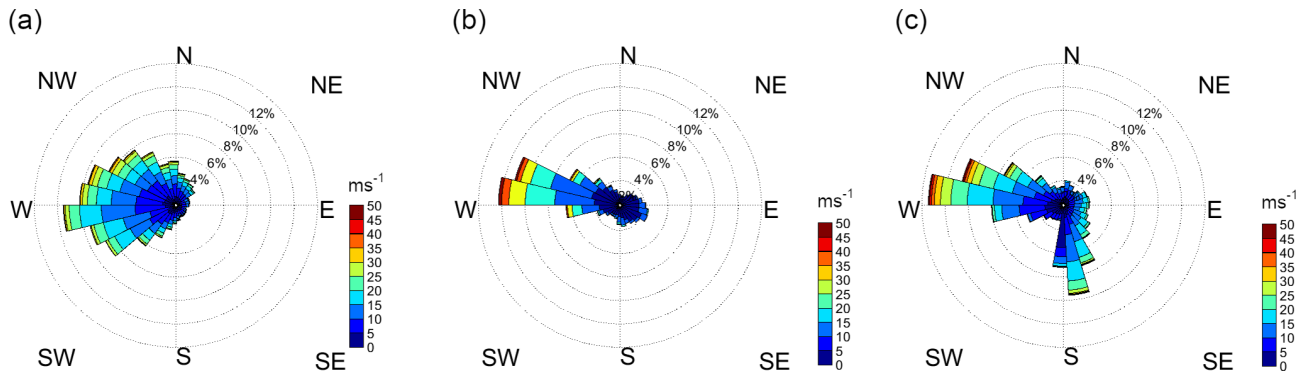
Figure 2. Wind roses at **(a)** 3975 m a.s.l., **(b)** 750 m a.g.l., and **(c)** 15 m a.g.l. at CRA over the period 2015–2022.

Strong synoptic forcing (wind speeds at 4000 m larger than $30 \, \text{m s}^{-1}$) mostly corresponds to flows in the westerly to northwesterly sector at altitude. Below the altitude of the Pyrenean crest and down to the surface, the airflow is usually channelled eastward.

The foehn phenomenon, typical of the lee of mountains (Elvidge and Renfrew, 2016), is very well observed at the CRA site. It is generated by synoptic southwesterly flows, generally associated with the approach of a front and with a low situated off the Bay of Biscay over the Atlantic. When the wind upstream of the mountain is strong enough, the foehn wind on the lee side can penetrate down to the surface (Scorer, 1955; Smith, 1985; Ólafsson and Bougeault, 1997). Oscillation of the whole troposphere is typically observed at CRA in a southwesterly synoptic forcing (Gueffier et al., 2024), generated by mountain lee waves (Bougeault et al., 1990; Ólafsson and Bougeault, 1997), with an occurrence of about 10 % (Gueffier et al., 2024). Note that the large occurrence of southerly winds in the wind rose of Fig. 2c includes the katabatic downslope winds from the Aure Valley, which are predominant at that height.

5.2 Seasonal variability

Figure 3 presents the seasonal and interannual variability of the monthly mean diurnal cycles of air temperature and water vapour mixing ratios (both at 2 m a.g.l.) at CRA and at PDM and of downward shortwave radiation (at the top of the 60 m tower) at CRA. The monthly composite days are shown separately for each year of the 2015–2022 period, which also highlights the interannual variability for a given month.

The downward shortwave radiation seasonal variability is typical of the mid-latitudes. June, July, and August are the hottest and most humid months, associated with the highest shortwave downward radiation. The diurnal cycle of temperature at CRA is marked in any month, even if it is of lesser amplitude in January and February. It is noticeable to see how it can remain high in September at the end of summer and be significant even in December in some specific warmer years. Those months often show anticyclonic dry and calm

conditions, with clear skies and a marked diurnal cycle. The diurnal cycle of moisture at CRA is less marked than that of temperature, partly because the composite is disturbed by non-diurnal variability like fronts or mesoscale advection.

It is interesting to notice the different behaviours of the diurnal cycles at PDM in relation to those at CRA. From April to October, the water vapour mixing ratio (temperature) shows a larger (smaller) diurnal amplitude at PDM than at CRA. This is likely due to the possible occurrence of a deep CBL at midday during this period that may overwhelm the PDM top during the daytime but leave it in the free troposphere during the night. On the contrary, in winter months, the PDM summit is mainly in the free troposphere, with a less marked diurnal cycle than during the rest of the year and than observed at CRA.

The interannual variability is usually large, often of the same order of magnitude as the diurnal variability (December and February are good examples of large interannual variability here), except in summer (it is very small in August for this period but might be larger for another period).

Figure 4 shows the seasonal variability of the cloud cover (monthly averages) based on the RAPACE total-sky imager and the ELIFAN algorithm (Lothon et al., 2019). The monthly standard deviation is expectedly large (not shown), about 40 % larger than the seasonal variability (less than 10 %). Still, April and May have, on average, larger cloud cover than September and October. Considering monthly averages calculated in the morning (between 3 and 4 h after sunrise) or in the afternoon (between 4 and 3 h before sunset) reveals a slight diurnal cycle, explained by a significant number of days with afternoon convection. Interestingly, this diurnal cycle vanishes in summer. This could be explained by the occurrence in summer of nighttime stratus clouds which dissipate in the late morning or afternoon, compensating for days with clear mornings but afternoon convection. Those stratus clouds can, notably, come from blocked northerly moist flows or from moisture coming from the daytime moist convection over the mountain, which is concentrated at the bottom of the valleys and the plain during the night. Summer
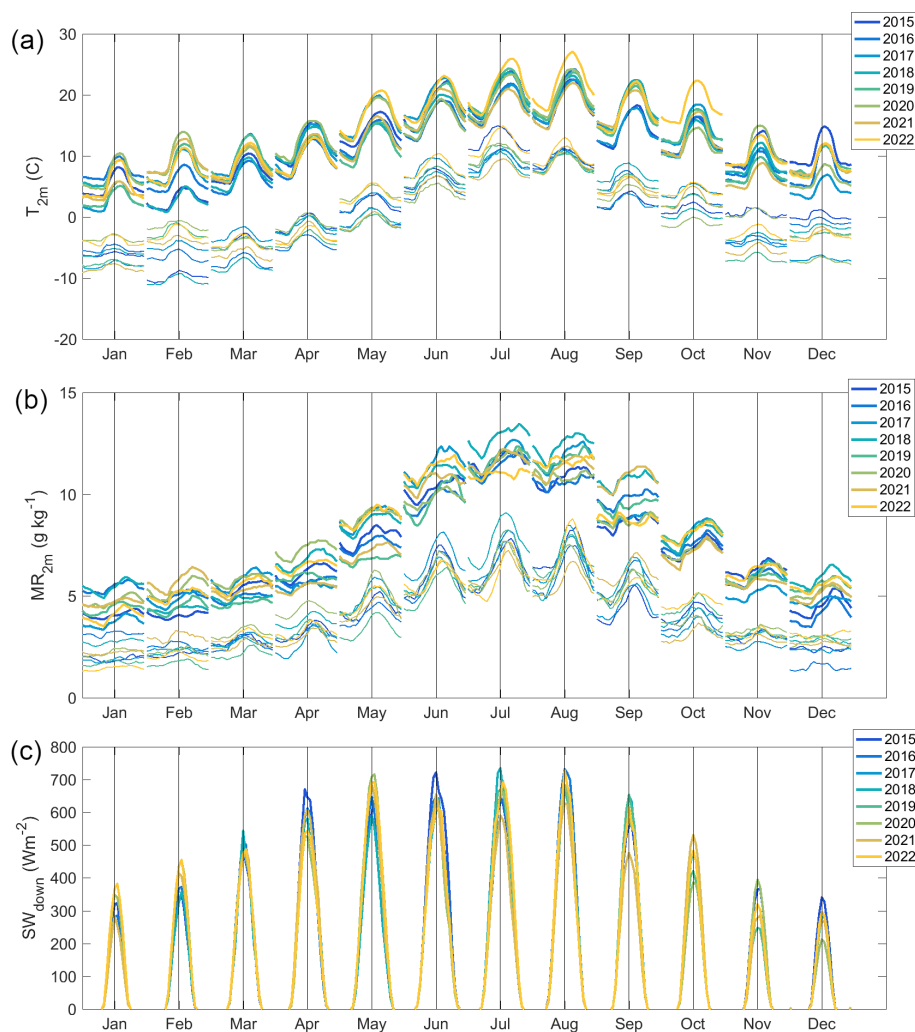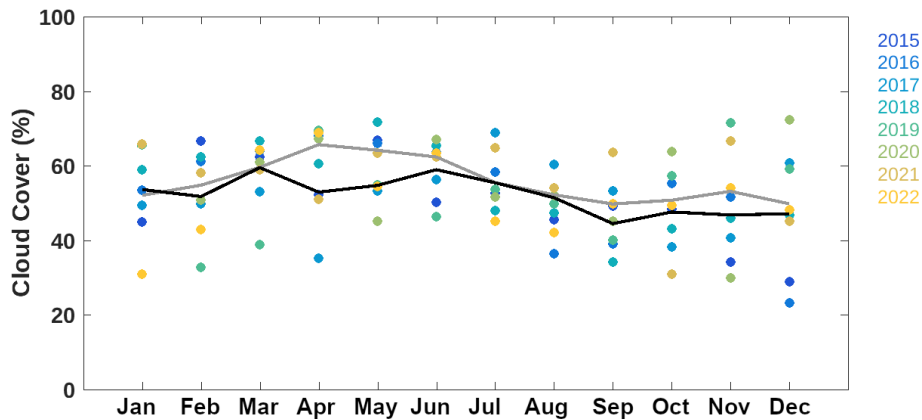
Figure 3. Seasonal and interannual variability of monthly averaged diurnal cycles of **(a)** 2 m temperature at (thick line) CRA and (thin line) PDM, **(b)** 2 m water vapour mixing ratio at (thick line) CRA and (thin line) PDM, and **(c)** downward shortwave radiation at CRA on top of the 60 m tower.

has a large occurrence of moist low layers in the northern Pyrenees, associated with a rather vegetated and moist surface, relative to the southern Spanish side. The diurnal cycle also disappears in winter, with the decreased shortwave radiation, drier air, and suppressed convection.

In Fig. 5, the precipitation values for the period 2015–2022 are shown through the mean monthly cumulative rain, the monthly mean rain rates for precipitation of more than $3 \, mm \, h^{-1}$, and the monthly maximum rain rate encountered. The use of those three variables enables us to distinguish between frequent low-precipitation events and convective intense-rain events. November, January, and February have the largest cumulative rain, associated with the largest number of rainy days. May, June, July, and August are the months with the highest maximum rain rates encountered, associated with convective storms. May and June have the largest mean rain rates when considering only significant rain events with

precipitation rates of more than $3 \, mm \, h^{-1}$. These months combine the chance of storms and the occurrence of moist blocked northerly flows. The driest months are September and October.

Figure 6 shows the convective boundary layer (CBL) depth Z_i estimated from the UHF wind profiler with the algorithm developed by Philibert et al. (2024) based on the detection of a local maximum in terms of the air refractive index structure coefficient and a minimum in terms of the vertical velocity standard deviation. The algorithm also takes temporal continuity into account. Note that only convective boundary layers are considered here, which implies that only cases with no rain and no fog allow for a CBL depth estimation. As expected, the cold winter months of November, December, and January have significantly smaller CBL depths relatively to other months. Spring and summer, interestingly, reach similar CBL depths despite the variations in incident
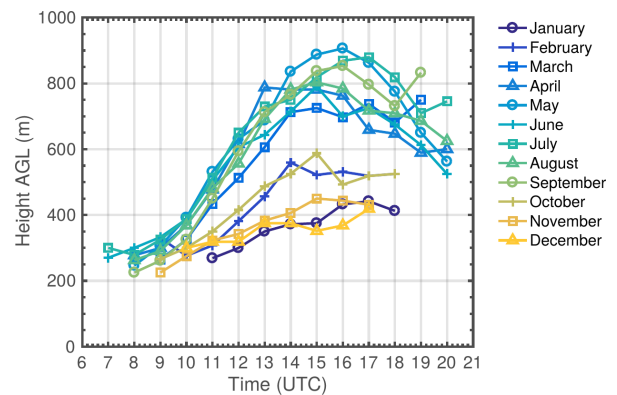
Figure 4. Seasonal and interannual variability of monthly averaged cloud cover for the period 2012–2019. Each dot is a monthly average. The black line is the average for morning hours (3 h after sunrise), and the grey line is the average for afternoon hours (3 h before sunset).
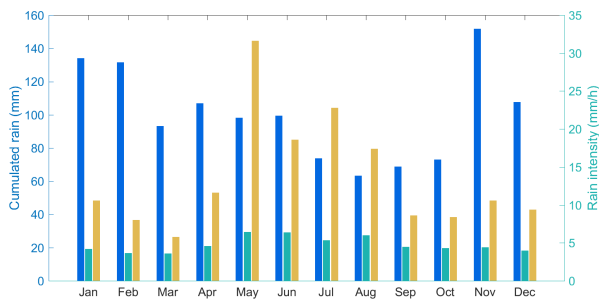
Figure 5. Monthly cumulative rain amounts (blue, left y axis), monthly mean rain rates for precipitation rates > 3 mm (green, right y axis), and monthly maximum encountered rain rates (brown, right y axis) for the 2015–2022 period at CRA.

Figure 6. Composite diurnal variation of CBL depth Z_i at CRA, averaged over 2015–2022, for each month of the year. Z_i estimates shown here were retrieved by use of CALOTRITON algorithm (Philibert et al., 2024).

shortwave radiation from one season to the other. This can be explained by several features. In summer, in the mountain area, the heating of the valley atmosphere is stronger than above flat terrain, mainly due to reduced volume (concept of topographic amplification; see Steinacker, 1984; Whiteman, 1990), and generates enhanced convection due to increased instability. Cumulus and congestus clouds develop actively all along the mountain ridge during fair-weather days, inducing a mesoscale subsidence near the mountain base (De Wekker, 2008). Therefore, the CBL at CRA is often capped by a significant subsidence (Pietersen et al., 2015; Blay-Carreras et al., 2014b) in this season, which limits the CBL growth. In April and May, convection is less active over the mountain, while the sensible heat flux can be as large as in summer or even larger because solar heating is significant while air masses are still cold (typically during post-frontal situations). This favours CBL growth. The month of September experiences similar CBL depth (and sensible heat fluxes) to April and May, with clearer skies and less rain being compensated for by a smaller temperature gradient close to the surface. February and October consistently show inter-

mediate CBL depths between the two groups of winter and summer. The standard deviation of Z_i within 1 month ranges from 100 to 500 m, with larger values in summer and at midday. It is around 300 m on average.

5.3 Long-term temperature trend

The unique PDM historical temperature time series built since the 1880s by the Observatoire Midi-Pyrénées and Météo-France were first studied by Bücher and Dessens (1991) and Dessens and Bücher (1995). Bücher and Dessens (1991) estimated an increase of $+0.83\,°\mathrm{C}$ in the temperature trend from 1882 to 1970. Dessens and Bücher (1995) revealed that, over the 100-year period (1882–1984), the daily maximum temperature decreased slightly by $0.5\,°\mathrm{C}\,(100\,\mathrm{yr})^{-1}$, while the daily minimum (nighttime) temperature increased significantly by $2.59\,°\mathrm{C}\,(100\,\mathrm{yr})^{-1}$. This means that the amplitude of the diurnal cycle decreased by about $2.9\,°\mathrm{C}\,(100\,\mathrm{yr})^{-1}$, which is very significant. They

showed that this temperature trend was associated with an increase in both the relative humidity and the cloud cover. Figure 7 shows an update to this long-term time series until 2020, along with the temperature measured at 2 m at CRA from 1991. Recent data (from 1984 onwards) used here come from the Météo-France synoptic stations at both sites.

Temperatures shown here are the annual mean of the daily minimum and maximum temperatures T_{min} and T_{max}, respectively, as well as the half-sum $\frac{1}{2}(T_{max} + T_{min})$, in order to remain homogeneous with the series studied by Dessens and Bücher (1995) and to be consistent with the international convention. This half-sum is conventionally used as being representative of the yearly averaged temperature.

At CRA, we can observe that the last 7 years (2014–2020) were all above the current temperature reference for this site, taken as the average over the period [1990–2000] (11.8 °C). A linear regression over the annual mean temperature series gives an increase in temperature of 1.1 ± 0.4 °C over the 30 years of measurements. However, the regression coefficient is only 0.26, and the period is not long enough to give a robust trend estimate.

At PDM, first of all, it is important to notice that the mean temperature exceeded zero in the 1980s. This has a strong impact on Pyrenean glaciers (Marti et al., 2015). A new linear trend estimate in relation to this series would give a trend of $+1.3 \pm 0.1$ °C $(100\,yr)^{-1}$ when calculated over the total period, $+0.9 \pm 0.2$ °C $(100\,yr)^{-1}$ for the first 100 years, and $+1.5 \pm 0.2$ °C $(100\,yr)^{-1}$ for the last 100 years. This is a significant difference that may reveal an acceleration of warming in the last 3 decades. However, caution needs to be taken since a period of 10 years is missing in the series from 1984 to 1994.

Note that compilation of historical ozone measurements shows an increase in tropospheric ozone by a factor 5 from the 1900s to the early 1990s (Marenco et al., 1994) but a stabilization around 45 nmol mol^{-1} from then and until the 2000s (Chevalier et al., 2007).

5.4 Atmospheric composition

Gas and particle measurements performed at PDM are, to some extent, representative of the air composition in the free troposphere (see discussion in Sect. 5.4). These measurements include reactive and greenhouse gases, as well as physical and chemical properties of suspended particles. In situ gas measurements are also available at the lowland site CRA (Table 1). As an illustration, Fig. 8 shows diurnal composites of ozone (ACTRIS-Fr), carbon dioxide (ICOS), and methane mole fractions (ICOS) and total suspended particle concentrations, separated on a seasonal basis. A 5-year period has been chosen to get averaged values with a good multi-annual representativity and optimized data coverage: January 2015 to December 2019 for PDM (consistent with the work by Gueffier, 2023 and Gueffier et al., 2024) and May 2019 to April

2024 for CO_2 and CH4 at CRA (as measurements started more recently there, in April 2019).[1]

Figure 8a (PDM) and 8b (CRA) commonly show that the ozone concentration is larger in spring and summer, linked with increased photochemical activity in the troposphere during those seasons (e.g. Chevalier et al., 2007). Further, the concentrations range between higher values in the free troposphere (Fig. 8a) than in the continental atmospheric boundary layer (Fig. 8b), as also evidenced for western Europe by Chevalier et al. (2007). At both sites, a diurnal cycle is visible in summer, but this is of lesser amplitude in spring and fall and almost absent in winter. The cycle at PDM (Fig. 8a) shows an ozone minimum short after noon but maximum values during the night, which is mainly due to the influence of anabatic transport from the valleys and the plain to the mountain summits. This had first been identified at PDM by Marenco (1986) based on a 1-year measurement campaign in 1982. This author raised the idea that air sampled at PDM during the warm season was a mix of boundary layer and free-tropospheric air, with proportions varying during the daytime, with free-tropospheric conditions being experienced during the night. The anabatic transport thus results in a decrease in ozone concentration during the daytime as the air from the lower levels is poorer in ozone relative to the free troposphere at the continental scale, as evidenced above. The anabatic-ozone decrease is stronger during the hot seasons, during which anabatic transport mostly occurs, and this is indeed typical of mountain summit observatories (Tsamalis et al., 2014). Concerning the plain site CRA (Fig. 8b), the ozone diurnal evolution is typical of the cycle most often observed in the continental boundary layer, with a maximum in the late afternoon and a minimum at sunrise. During the night, the ozone decay in the stable boundary layer is due to ozone surface deposition (and possibly due to ozone titration by NO, but NO concentrations are expected to be low in this rural area). As soon as the sun rises, entrainment of higher concentrations of ozone from aloft within the growing convective boundary layer contributes to making ozone concentration grow near the surface (as illustrated in Tsamalis et al., 2014). Photoproduction can also contribute to the daytime ozone build-up, but further investigation is needed to assess this contribution, taking into consideration the local NO_x measurements.

The influence of anabatic transport was studied specifically for PDM by Gheusi et al. (2011), Tsamalis et al. (2014), and Hulin et al. (2019). These studies further illustrate that it affects other atmospheric species as soon as a vertical concentration gradient exists in the regional background atmospheric profile. This is the case for carbon dioxide (CO_2), which undergoes a similar influence (Fig. 8c): during the daytime, the anabatic upflows transport air depleted in CO_2

---

[1]Due to the rapid multi-annual anthropogenic trend of CO_2 and CH$_4$, the absolute values presented here for PDM and CRA over different periods should not be compared.
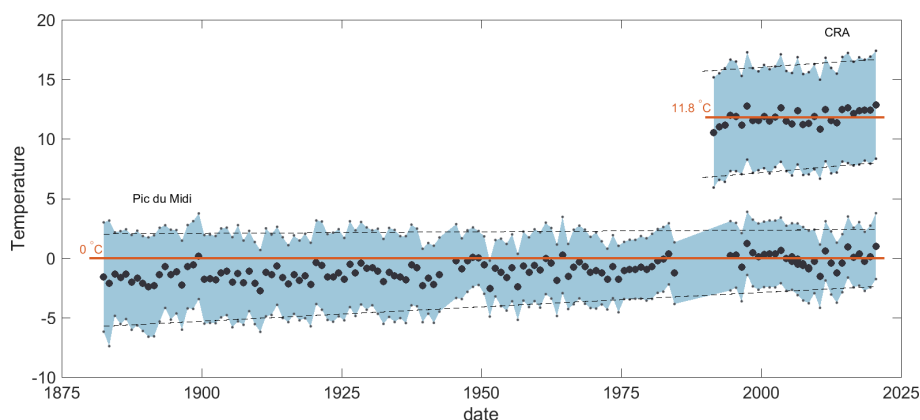
Figure 7. Long-term series of the annual mean of daily minimum and maximum temperatures at PDM and CRA (small dots and envelop). Bold dots represent $\frac{1}{2}(T_{max} + T_{min})$. The level of 0 °C is indicated for the historical series of PDM as being indicative of the retreat of glaciers at this altitude in the Pyrenees. The level of 11.8 °C is indicated as the temperature reference for CRA, which is the averaged temperature over the period [1990–2000]. For each minimum or maximum temperature time series, linear regression is indicated with dashed lines. Slopes are 2.4 and 0.3 °C $(100\,\mathrm{yr})^{-1}$ and 1.2 and 0.9 °C $(30\,\mathrm{yr})^{-1}$ for, respectively, the PDM minimum and maximum temperature and the CRA minimum and maximum temperature.

relative to free-tropospheric air at the height of PDM due to increased photosynthetic activity near the surface in the valleys and the plain. This again results in a marked diurnal cycle of CO_2 during summer, one of weak amplitude in spring and fall, and almost no diurnal variability during winter. Such influence is also observed at other mountaintop observatories in the world (e.g. Necki et al., 2003). At the seasonal scale, the tropospheric background in CO_2 decreases as the photosynthetic activity increases during the vegetation season, and so concentrations are at their maximum in winter and at their minimum in summer. Note that a multi-annual increase of about 2 ppm per year was estimated for CO_2 at PDM over the period 2015–2019 by Gueffier et al. (2024), which is consistent with the global anthropogenic trend observed worldwide (Friedlingstein et al., 2023). CO_2 measurements at CRA (Fig. 8d) show similar seasonal trends as at PDM with respect to the absolute CO_2 levels. Nevertheless, the amplitude of the diurnal cycle is wider, especially in summer. Nighttime CO_2 build-up is observed until sunrise, presumably due to soil respiration and CO_2 accumulation near the ground in the stable boundary layer. This idea is supported by stronger CO_2 concentrations being found at 30 m than at 60 m above the ground during the night. After sunrise, mixing within the developing convective boundary layer dilutes the CO_2 previously accumulated near the ground, and the CO_2 curves at 30 and 60 m tend to overlap during the day.

In the P2OA rural and mountainous region, methane (CH_4) mainly comes from agricultural activity. However, oxidation of methane by OH radicals results in a seasonal decrease in CH_4 when oxidation is most important (Necki et al., 2003). This explains the maximum in the methane concentration in winter and the minimum in summer (Fig. 8e). Similarly to other mountain observatories (Necki et al., 2003),

CH_4 at PDM displays a marked diurnal cycle in summer, with a maximum in the daytime, here again related to transport by anabatic flows, conveying air richer in CH_4 from the lowlands. This diurnal cycle is again less pronounced in spring and fall and absent in winter, which is consistent with the seasonal variability of the occurrence and the intensity of thermally driven circulations at PDM (Hulin et al., 2019).

As at high Alpine sites, anabatic transport at PDM (Fig. 8f) is one of the most decisive factors contributing to aerosol concentration variability (Collaud Coen et al., 2011; Herrmann et al., 2015). Still, for comparison, Sun et al. (2021) also showed that, at Zugspitze–Schneefernerhaus (2671 m) and Jungfraujoch (3580 m), higher concentrations and stronger diurnal variability were observed in the warm season, while lower concentrations and less distinct diurnal variability were observed in the cold season.

6   Illustrative studies based on P2OA

In this section, we present examples of various applications of P2OA dataset and experimental sites with regard to the following:

– atmospheric-process studies based on the long-term series or on hosted field experiments (Sect. 6.1)

– instrumentation test campaigns (Sect. 6.2)

– evaluation of numerical weather prediction models (Sect. 6.3).

All field experiments hosted at P2OA are listed online (https://p2oa.aeris-data.fr/field-campaigns/, last access: 16 October 2024), with indications of the hosting site (PDM, CRA, both), addressed scientific topic, and involved research
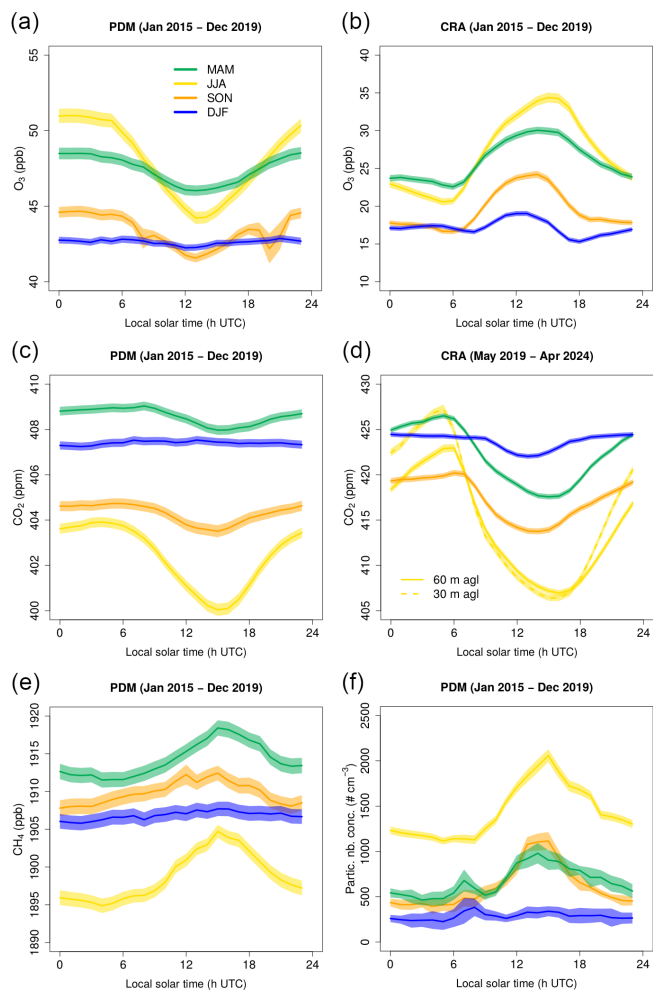
Figure 8. Composite diurnal cycle by season of mole fractions of **(a–b)** ozone, **(c–d)** carbon dioxide, **(e)** methane, and **(f)** total suspended particle number concentration observed at PDM **(a, c, e, f)** and at CRA **(b, d)**: DJF refers to December–January–February, MAM refers to March–April–May, JJA refers to June–July–August, and SON refers to September–October–November. In panel **(d)**, all curves represent air taken at 60 m a.g.l., except for the dashed JJA curve representing air taken at 30 m a.g.l. The uncertainty ranges correspond to plus or minus the standard error of the sample. Mean values are considered in panels **(a)–(e)**, but median values were preferred in panel **(f)** due to the distribution skewness for particles.

laboratories. Here, in the following subsections, we focus on a few chosen projects or studies that are illustrative of the scientific potentials of P2OA.

6.1 Process studies

6.1.1 Surface–atmosphere interaction

The instrumentation of P2OA – and, in particular, at CRA – is especially appropriate for the study of the atmospheric boundary layer dynamics and surface–atmosphere interac-

tions. In 2011, an international field experiment was hosted at P2OA for the study of the transition from the daytime convective boundary layer to the stable nocturnal boundary layer: the Boundary Layer Late Afternoon and Sunset Turbulence (BLLAST: Lothon et al., 2014, https://bllast.aeris-data.fr, last access: 16 October 2024). This transitional phase of the diurnal cycle was the unique focus of this project and field campaign. Over 3 weeks, research groups from Europe and the USA gathered a large number of complementary devices in order to densely observe the atmospheric boundary layer from the surface to the top and from midday to the night. Radiosoundings, tethered balloons, manned aircraft, and unmanned aeroplanes were operated over 12 favourable days, and continuous measurements were conducted with instrumented towers deployed over various vegetation covers and with remote sensing devices (lidar, sodar, radiometer, ceilometer, camera), which were all added to the existing permanent instrumentation. From the collected dataset, a fine description of the turbulence decay was obtained (e.g. Lothon et al., 2014; Darbieu et al., 2015; Nilsson et al., 2016a, b), which revealed how the decay remains normalized and faithful to the Deardorff model quasi-stationarily until the surface flux becomes too small to maintain the mixing. Starting then, the turbulence decay gets faster, and the turbulence structure changes, with larger turbulence scales in the boundary layer and smaller turbulence scales in the surface layer. The shape of the energy spectra also changes. It was also shown that a pre-residual layer can be defined before the residual layer overlying the stable nocturnal layer. This pre-residual layer corresponds to a layer between the top inversion and the top of the turbulence layer coupled to the surface. At that time, again, the surface fluxes are not strong enough to maintain the mixing up to the top inversion and previous daytime convective boundary layer top. The scheme in Fig. 9 summarizes those findings. In this figure, time is represented with normalized dimensionless time $\hat{t}$, which is typical in turbulence decay studies (Nadeau et al., 2011). $\hat{t}$ is based on the period from maximum to null buoyancy flux:

$$\hat{t} = \frac{t - t_{\max}}{t_{\text{zero}} - t_{\max}}, \tag{1}$$

where $t_{\max}$ is the time during mid-day when the surface buoyancy flux is at maximum, and t_{zero} is the time when the surface buoyancy flux gets to zero later in the day. Thus, $\hat{t}$ equals zero at maximum buoyancy and 1 at zero buoyancy flux. Several other features were finely studied, revealing, for example, the importance of the advection of small-scale heterogeneities (Cuxart et al., 2016); the mystery of the lifted temperature minimum a few tens of centimetres above the surface during the stabilization process (Blay-Carreras et al., 2015); the difficulty in scaling the turbulence decay (Nilsson et al., 2016a; El Guernaoui et al., 2016); the occurrence of counter-gradient heat fluxes (Blay-Carreras et al., 2014a); the uncertainty of Monin–Obukhov similarity theory (MOST) (Kooijmans and Hartogensis, 2016); or the interac-
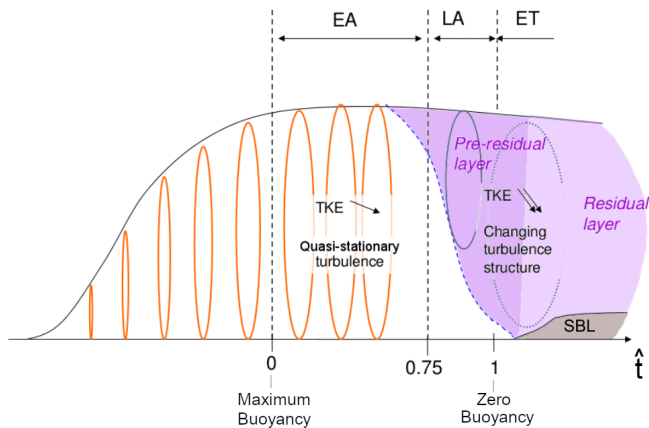
Figure 9. A scheme of the atmospheric boundary layer diurnal cycle and turbulence structure evolution, based on the results of the BLLAST project (Lothon et al., 2014). $\hat{t}$ is normalized dimensionless time. EA refers to the early afternoon, LA refers to the late afternoon, and ET refers to the evening transition. TKE refers to the turbulent kinetic energy, and SBL refers to the stable boundary layer. Ellipses represent the structure, size, and coupling of vertical velocity eddies.

tions between the drainage flows, gravity waves, and turbulence (Román-Cascón et al., 2015).

BLLAST only slightly addressed the role of surface heterogeneity, while the latter raised several questions, not only during the afternoon transition but also more generally. In 2023, P2OA hosted a new field experiment focused on the impact of surface heterogeneity on the atmosphere: the MOSAI project (Model and Observation for Surface-Atmosphere Interactions, https://mosai.aeris-data.fr/, last access: 16 October 2024, Lohou et al., 2023). MOSAI addresses three questions :

– What is the representativeness of the 60 m tower flux measurements or other permanent measurements with respect to the surrounding heterogeneous landscapes (prairies, forests, crops, and small villages)?

– How can we develop appropriate methodologies to evaluate the NWP and climate models based on surface–atmosphere interactions?

– Can we improve the representation of surface–atmosphere coupling in NWP and climate models?

To address those questions, three 1-year field experiments were planned at three instrumented sites in France: Meteopole in 2021 (Canut et al., 2019), SIRTA in 2022 (Haeffelin et al., 2005), and P2OA in 2023. Each time, the four or five most representative vegetation covers of a 5 km × 5 km model mesh around the permanent tower were instrumented with surface flux towers. In 2023, at P2OA, three 15 d intensive observation periods (in April, August, and December) were added for the study of a forest-to-culture transition

with a tethered balloon, remotely piloted aeroplane systems (RPASs), and several towers instrumented at different levels above and within the forest. This should enable us to finely study the vertical structure of the local transition, with different sublayers (internal boundary layer, equilibrium boundary layer, etc.; Bou-Zeid et al., 2020).

6.1.2 Atmospheric composition

Impact of meteorology on atmospheric composition at PDM

It has been long recognized (e.g. Keeling et al., 1976) that atmospheric-composition measurements conducted on top of high mountains are better representative of the troposphere at the global scale than continental low-altitude stations, which undergo local influences. Comparing ozone mole fractions measured at PDM and other mountain stations in Europe on the one hand with airborne measurements in the free troposphere on the other hand, Chevalier et al. (2007) indeed found agreement within 8 % with the reference airborne profiles for stations above 2000 m a.s.l., provided multi-year averages were considered.

Summit observatories may, nevertheless, be influenced, at least part of the time, by local or regional emissions transported by boundary layer processes. Two field campaigns – Pic 2005 and Pic 2010 – were designed to address this question for PDM. Pic 2005 (Gheusi et al., 2011) revealed that, during summer fair-weather days, ozone measurements in the daytime at PDM were representative of the mixing of layers present between 1000 and 2000 m a.s.l. above the Pyrenean foreland (CRA). By means of a Lagrangian transport model integrating ozone photochemistry, Tsamalis et al. (2014) showed, for 2 fair-weather days during Pic 2005, that the best adjustments to observed ozone diurnal variations at PDM were obtained when 14 % to 57 % (depending on the day) of air from the boundary layer was incorporated into free-tropospheric air before reaching PDM.

During Pic 2010, meteorological and ozone radiosoundings were launched simultaneously from CRA and from a valley bottom very close to PDM (Hulin et al., 2019). These profiles allowed the characterization of a humid venting layer formed during the daytime above the Pyrenees by anabatic pumping of low-level air and then exported above the plain by the altitude return branch of the plain-to-mountain breeze below 2000 m. Here, this is well illustrated by a numerical simulation of an anabatic day (Fig. 10). In such conditions, PDM appears to be influenced during the afternoon by local weak southerly wind (which is typically observed) conveying the Pyrenean venting layer towards the plain.

To put the above studies in their climatological context, Hulin et al. (2019) also explored the occurrence of thermally driven circulations at P2OA over a 10-year period (2006–2015), along with their impact on air composition at PDM. Methods to detect thermal circulations in the P2OA area al-
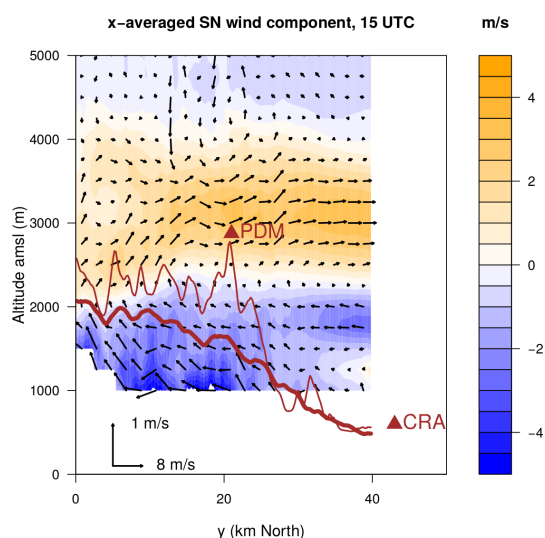
Figure 10. High-resolution (200 m) simulation with Meso-NH (Lac et al., 2018) of a typical sunny afternoon in summer with a well-developed plain–mountain thermal circulation (10 July 2010, 15:00 UTC, with PDM being located at the centre of a $40 \times 40\,km^2$ domain). This south–north vertical cross-section (y–z plane) shows model fields averaged over 40 km along the zonal (x) direction. The vectors show the projection of the (x-averaged) wind on the section plane, while the colour code emphasizes the y component. The thin brown line shows the terrain profile at the longitude of PDM, while the bold line represents the x-averaged terrain elevation in the model domain. PDM (represented at its real altitude) peaks markedly above the x-averaged terrain altitude but only 100 m above the model terrain at this location.

lowed us to separate ensembles of days with or without anabatic influences at PDM, revealing contrasted diurnal evolutions of the observed atmospheric species (consistently with the diurnal composites shown in Fig. 8).

Gueffier et al. (2024) went beyond the specific influence of thermally driven circulations and explored more generally the influence of synoptic meteorology on air composition at PDM. Considering 5 years of meteorological data collected at P2OA (2015–2019), weather regimes were distinguished by hierarchical clustering. The most characteristic ensembles that emerged were days of fair, calm weather (favourable to thermally driven circulations), disturbed weather with westerly advection, and southern foehn conditions. Marked differences were found between the meteorological clusters when considering the air contents in Rn, O_3, CO, CH_4, CO_2, and particles. Among other results, it was shown that (i) air driven to PDM by southern foehn had mostly a free-tropospheric signature; (ii) despite enhanced anabatic influence, the regional free-tropospheric influence remains dominant during anticyclonic fair-weather days; (iii) disturbed weather caused intense mixing of the lower troposphere at the regional scale, and, thus, the influence of regional emission sources is stronger.

Aerosol properties

Guillaume et al. (2008) succeeded in simulating with a global model (ORISAM-TM4, Guillaume et al., 2007) the temporal evolution of black carbon (BC) and total organic carbon (OC) in the aerosol measured at PDM from weekly filter samples. They thus showed that large-scale BC pollution is most prominent at this site compared to possible local influences, especially during heatwaves, such as the major one during the 2003 summer. In addition, formation of secondary organic aerosols was found to be a major component of OC in such meteorological conditions.

As indubitable evidence of hemispheric transport to PDM, radioactive fallout due to the explosion of three reactors of the nuclear power plant in Fukushima (Japan) on 12–15 March 2011 was detected at PDM in an aerosol filter sample (Evrard et al., 2012). The presence of 131-iodine in aerosols ($200 \pm 6\,\mu Bq\,m^{-3}$) indicated that the radioactive cloud reached France between 22 and 29 March, i.e. less than 2 weeks after the initial emissions, as the IRSN measurement devices also indicated.

More recently, Tinorua et al. (2024) performed a study based on 2-year measurements (2019–2020) of BC microphysical and optical properties at PDM using specific instruments to complement the ACTRIS instrumental set. They showed that, among the existing long-term monitoring sites worldwide, PDM experiences only occasional influences by the planetary boundary layer, making it an ideal site for characterizing free-tropospheric BC. Moreover, their classification of the dominant aerosol type using the spectral aerosol optical properties indicated that BC was the predominant absorption component of aerosols at PDM and controlled the variation of single-scattering albedo throughout the 2 years.

Greenhouse gases

P2OA is part of the national ICOS-France network, but PDM and CRA not yet labelled as European ICOS-ERIC stations. They, nevertheless, both contribute to the European datasets compiled annually by ICOS for CO_2 (Bergamaschi et al., 2024a) and CH_4 (Bergamaschi et al., 2024b). In particular, the PDM station was at the heart of the evaluation of the method for the spike detection algorithm which is now applied to all the stations in the ICOS network (El Yazidi et al., 2018; Tenkanen et al., 2021; Cristofanelli et al., 2023). P2OA data have also been used to study the impact of European droughts on the CO_2 concentrations and fluxes (Ramonet et al., 2020; Thompson et al., 2020; He et al., 2023), as well as to study global and European methane balances (Saunois et al., 2020; Szénási et al., 2021; Thompson et al., 2021).

Atmospheric mercury

Mercury (Hg) is a heavy metal that is dispersed globally in the gas phase following its emission from volcanoes and

human activities. The atmospheric lifetime of Hg is not well constrained due to its complex redox chemistry, making model predictions of Hg deposition and ecosystem loading difficult. At P2OA, we have generated from 2010–2014 one of the longest high-altitude atmospheric Hg datasets, using automated instruments that quantified gaseous elemental Hg(0), gaseous oxidized Hg(II), and aerosol Hg(II) dynamics at a 2 h resolution (Fu et al., 2016a; Maruszczak et al., 2017). Together with experimental rainfall Hg photoreduction rates (Yang et al., 2019), these data have helped to better constrain atmospheric Hg redox reactions in global Hg chemistry and transport models (Saiz-Lopez et al., 2018). We have also developed unique methods to sample and measure the stable isotope composition of atmospheric Hg(0) and Hg(II) in gases, aerosol, and precipitation, which inform us about deposition pathways and fluxes (Fu et al., 2016b, 2021; Enrico et al., 2016). The data are freely available through the AERIS/GMOS and iGOS4M data hubs (see Table B1).

Microplastics and other trace species

P2OA also hosted punctual campaigns on the atmospheric chemistry and transport of diverse environment-impacting species such as halogens and selenium (Suess et al., 2019), formaldehyde (Prados-Roman et al., 2020), and microplastics (Allen et al., 2021). Over a period of 4 months in summer 2017, polymer fragments and fibres ranging in size from 3.5 to 53 μm were observed at relatively low (0.25 microplastics m^{-3}) but significant levels. The polymers identified, namely polyethylene, polystyrene, polyvinyl chloride, polyethylene terephthalate, and polypropylene, are all known for their use in packaging. The origin of these microplastics has been studied by back-trajectory modelling of the air masses observed at PDM. Many of these trajectories have their origin in Africa, the Atlantic Ocean, and North America, indicating that an intercontinental transport is at the origin of the microplastics detected at PDM.

6.1.3 Exploring transient luminous events

In the late 1980s, a new field of research opened with the discovery of transient luminous events (TLEs), which now include sprites, "ELVES" (Emission of Light and Very-Low-Frequency perturbations due to Electromagnetic Pulse Sources), jets, and other electrical phenomena occurring above thunderstorms (Füllekrug et al., 2006). The first European TLE-dedicated observations were obtained at PDM in 2000 (Neubert et al., 2001). In the following years, several European teams joined euroSPRITE during the summer and autumn, campaigns leading to over 700 TLE images being captured in the period from 2000 to 2008 (Neubert et al., 2008). The two observation sites of P2OA, equipped with a remote-controlled sensitive camera system, contributed to a climatology of TLEs in Europe (Arnone et al., 2020) and a

large number of process studies (e.g. Soula et al., 2015, 2017; Gomez Kuri et al., 2021; Tomicic et al., 2021).

During five successive nights from 16 to 21 January 2017, several storm systems over the Mediterranean Sea, highly productive in TLEs, were monitored with the camera at PDM. A total of 589 TLE events were recorded and analysed in the thesis by Gomez Kuri (2021). This large number of TLEs and the diversity of the storm systems capable of producing TLEs allowed us to support previous observations and/or to reinforce some theories on the mechanisms and conditions of their production. Figure 11 shows the continuity of the cloud-to-ground (CG) lightning flash activity observed by PDM with the METEORAGE network (https://www.meteorage.com/fr/, last access: 16 October 2024) during 5 d of the winter period within the region pointed at by the camera. There was an increasing flash rate during several cycles, corresponding to individual cells at the beginning of the period and an evolution to larger developments of storms, such as mesoscale convective systems in the second part of the period. The TLEs were observed over the five nights, with specific time intervals being more favourable to some TLE categories, like ELVES (green histogram in Fig. 11) when the cloud-to-ground flash rate was large (around 20:00 UT on 20 January) and sprites (red histogram) a few hours later while the flash rate decreased substantially. The analysis of the location of each TLE in its storm context shows that sprites were often produced over stratiform regions of mesoscale convective systems during their dissipating stage and were associated with a positive stroke, the peak current of which was, on average, about 107 kA. ELVES mainly occurred in systems of strong convection during the mature stage, which produced negative strokes of high peak current. ELVES are more likely to occur with clouds that have large vertical but small horizontal extensions, whereas sprites occur over clouds of smaller vertical but larger horizontal extensions (Gomez Kuri, 2021). On the night of 19 January, out of 106 TLEs observed above a mesoscale convective system developing between the south of Ebro delta and the Balearic Islands, 97 % of 29 elves occurred over sea while 45 % of sprites occurred over land. This is in accordance with other observations and with larger peak current values for strokes over sea.

6.2 Instrumental and methodological validation

The rich panel of instruments and infrastructures of both sites makes P2OA a hosting platform suitable for research groups to test new instruments or sensors, which can be compared to reference measurements of the permanent instrumentation. Here, we give two examples of such experimentations.
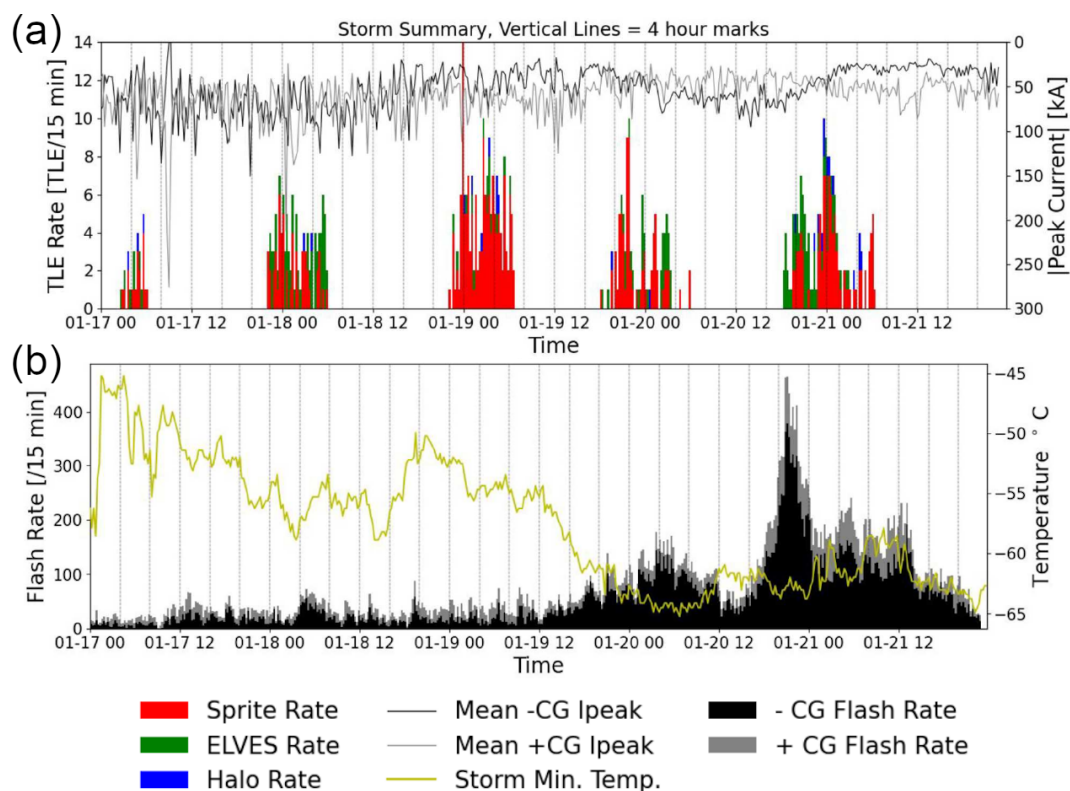
Figure 11. TLE recorded at PDM and cloud-to-ground (noted as "CG" here) lightning flash activity between 17 January, 00:00 UTC, and 22 January, 00:00 UTC (from Gomez Kuri, 2021). **(a)** TLE rate over 15 min intervals (histograms) and mean negative and positive peak current of cloud-to-ground strokes in the same time intervals (black and grey lines, respectively). **(b)** Cloud-to-ground flash rates (negative and positive with black and grey histograms, respectively) and the minimum cloud top temperature over the area of study over 15 min (green line). The minimum cloud top temperature is issued from the thermic infrared channel of the Spinning Enhanced Visible and Infrared Imager radiometer on board the Meteosat Second Generation thanks to the French AERIS/ICARE Data and Services Centre.

6.2.1 Instrumented RPAS and balloon experimentations

With its open spaces (70 ha) mainly being composed of prairies, its instruments on atmospheric boundary layer dynamics, and its infrastructure (hangar, storage buildings, mechanical and electrical workshops, meeting and working rooms, lodging), CRA is particularly appropriate for balloon and RPAS operations and airborne instrumentation tests. In total, about 30 test campaigns involving light aircraft and airborne instruments have been hosted at P2OA since 2015, either with a tethered balloon or with RPAS (free radiosounding balloons are not counted here). In the context of aerial activities and regulation, a temporary regulated area is activated for those operations when needed. The goal of the field campaign is either to test the flying vector, the fly strategy, or new sensors. Thus, P2OA was the test site of RPAS and sensor pre-campaigns before international or national field experiments like BACCHUS (Calmer et al., 2019), NEPHELAE (Hattenberger et al., 2022), EUREC4A (Elucidating the role of cloud-circulation coupling in climate, Maury et al., 2023). The strategies of fleet flying (Hattenberger et al., 2022), cata-

pult take off, and thread landing have been tested. Sensors for turbulence measurements (Calmer et al., 2018; Alaoui-Sosse et al., 2019, 2022) have been validated based on the P2OA 60 m tower turbulence measurements.

Earlier, during BLLAST, several new observational devices or methodologies were tested or enabled: a technique of frequently launched radiosoundings with a line-cutting system and re-usable probes (Legain et al., 2013); the SUMO RPAS, which is a light tool for frequent profiling of meteorological variables (Reuder et al., 2016) and turbulence (Båserud et al., 2016); a turbulence probe on board a tethered balloon (Canut et al., 2016); and a method for estimating heat fluxes based on frequent profiling of the atmosphere (Båserud et al., 2020).

6.2.2 Improvement of airborne gamma-ray techniques for radiological surveys and environmental applications

Gamma-ray spectrometry allows the identification and quantification of natural (U- and Th-decay products, ^{40}K) and artificial (e.g. ^{137}Cs) radionuclides in the environment. Mon-

itoring their time and space variations offers the possibility to study the environmental factors responsible for these variations, such as soil humidity content and vertical profiles (which have an effect on gamma-ray attenuation), surface–atmosphere gas exchange, atmospheric boundary layer dynamics and synoptic transport (which modulate radon flux and atmospheric concentration), dry and wet aerosols' scavenging (which affects the vertical distribution of atmospheric radon decay products), and migration of radionuclides in soils. A suite of instruments dedicated to these studies was deployed at CRA by CEA/DAM and IRAP from 2018 to 2019: a 20 L NaI(Tl) RSX-5 spectrometer mounted on top of CRA's 60 m tower, atmospheric and soil radon monitors (three AlphaGUARDs at 1, 30, and 60 m and three BARASOL probes at depths from 15 to 90 cm in the ground) and time domain reflectometry soil humidity probes. A specific application consisted of quantifying the influence of environmental parameters (atmospheric radon, soil moisture, cosmic radiation, atmospheric pressure) on the measurement of natural and artificial radioactivity by means of airborne gamma-ray spectrometry (Amestoy et al., 2021) in order to improve the surveying of sites with nuclear activities or radioactive fallouts and to characterize the evolution of surface deposits by remote sensing systems such as the HELINUC™ system developed by CEA/DAM (see Fig. 12). A campaign was conducted to monitor the combined evolution of these parameters over 14 months combined with several helicopter flights over CRA and resulting in the correction and validation of the protocol for airborne gamma-ray spectrometry (called PAS-THEL) that leads to high measurement precision (Amestoy, 2021). The simulation of a hovering flight by installing the NaI(Tl) spectrometer at 50 m on the 60 m tower made it possible to continuously measure natural radioactivity at a fixed point, focusing on environmental temporal variations. The addition of atmospheric-radon detectors made it possible to understand the dynamics of this radioactive gas and its influence on the gamma-ray signal. The installation of time domain reflectometry probes, the study of satellite images, and the use of a pluviometer allowed the quantification of the influence of soil moisture and rainfall on the gamma-ray signal. Thus, the effects of atmospheric radon, soil moisture, and rainfall could be characterized and taken into account to restore the gamma signal representative of the site's natural radioactivity.

6.3 Evaluation of numerical weather prediction models

The multi-instrumental long-term series of P2OA give solid opportunities to evaluate numerical models on specific issues. Three examples are given in this section.

6.3.1 Atmospheric-dynamics variability

As mentioned before, mountain lee waves are typical of the area, generated by southwesterly flow over the Pyrenees. The marked oscillations of the vertical velocity within the whole troposphere that is associated with them; the complex cloud cover system formed; and the impact on the temperature, moisture, and transport of chemical species are all difficult to capture in a numerical model, mostly due to the complexity of the terrain itself and due to the challenge of taking the subgrid topography into account.

The measurements of the VHF wind profiler radar at P2OA enable us to test the ability of NWP models to simulate the dynamics of the atmosphere in such cases. In particular, the vertical velocity observed by the radar in the mid-troposphere can reach absolute values larger than 2 m s^{-1} during foehn events, while it is usually smaller than 30 cm s^{-1} in other situations (except convective storms). Large vertical velocity variance can thus be observed over a few hours in the case of mountain waves in southerly flows relative to other typical synoptic situations. The use of a threshold with regard to vertical velocity variance is actually one possible diagnostic of their occurrence (Gueffier et al., 2024). Note that the VHF measurements correspond to rather large scales: a few kilometres horizontally (depending on height, due to beam divergence) and 375 m vertically.

One way to statistically evaluate the NWP models with regard to this aspect is to compare the observed and modelled density energy spectra of the vertical wind component. The two Météo-France NWP models are considered here, from which profiles are continuously extracted from the P2OA location for model evaluations: ARPEGE (7 km horizontal resolution, Courtier and Geleyn, 1988) and AROME (1.3 km horizontal resolution, Seity et al., 2011). For AROME, 16 atmospheric columns are averaged around the CRA site, and 3 are averaged for ARPEGE. Model outputs are extracted at 1 h time resolution. Figure 13 shows the normalized energy density spectra of both the zonal component of the wind (Fig. 13a) and the vertical velocity (Fig. 13b) for a 4-month period of 2018, from January to April. This period was chosen as it is long enough for this typical comparison example and because there is no gap in the observational data. The chosen altitude is close to 3000 m a.s.l., which is that of the highest peaks at the border. It remains representative of the process since the whole troposphere, from 1 km or below up to 8 km or above, coherently oscillates vertically during mountain wave events (Gueffier et al., 2024).

Figure 13a first shows that the two models correctly represent the variability of the horizontal wind at timescales ranging from 1 h to 1 month. At large synoptic scales, ARPEGE and AROME are very similar, consistently with the forcing of AROME with ARPEGE. They depart slightly from observations around the scale of 30–40 d, which is difficult to interpret. Consistently with their horizontal resolution, ARPEGE departs slightly from the observations at scales smaller than 1 d, while AROME is remarkably faithful to the observations at scales smaller than 1 d.

Based on the quality of horizontal wind spectra, one can now consider the vertical velocity variability. Figure 13b re-
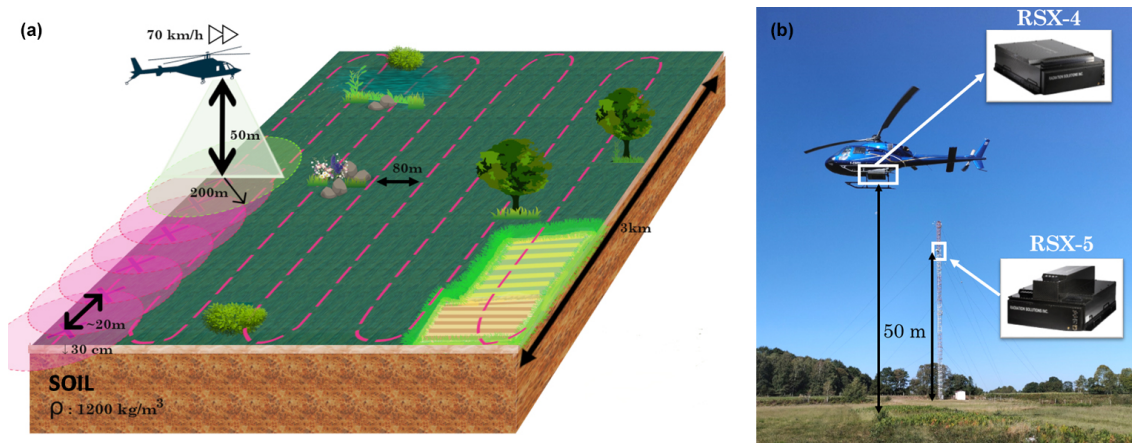
Figure 12. (a) Principle of airborne gamma-ray spectrometry. **(b)** Simultaneous acquisition between the onboard spectrometer (RSX-4) and the one installed on the 60 m tower (RSX-5) at CRA, 8 September 2020.
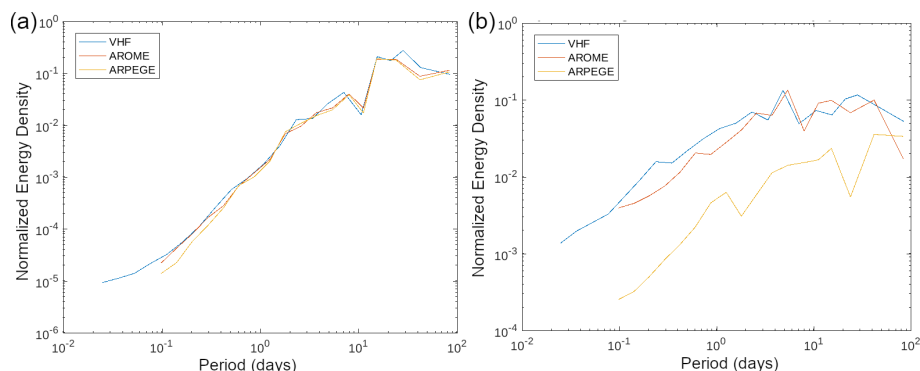
Figure 13. Normalized energy density spectra of **(a)** the zonal component of the wind and **(b)** the air vertical velocity at the altitude of 3325 m a.s.l., as observed by P2OA VHF wind profiler radar, modelled by AROME and modelled by ARPEGE, over the 4-month period of January to April 2018.

veals how much lower the energy is in ARPEGE: the coarser model is not able to represent the variability of the vertical velocity at any timescale, with the energy density being about 10 times smaller than observations. Among other processes, it always strongly underestimates the oscillations of the troposphere during foehn or mountain wave events (not shown), which occur around 10 % of the time (Gueffier et al., 2024). The finer model, AROME, however, much better represents the vertical velocity variability. It has, globally, a very satisfying energy density level, even if it slightly underestimates the variance at timescales smaller than 2 d.

This example shows the potential of the 20-year-long VHF wind profiler dataset for evaluation of the NWP models and the studies of dynamical processes that are typical of mountain regions.

6.3.2 Surface fluxes

As outlined by the MOSAI project (see Sect. 6.1.1), there is a clear need to dig into the representation of surface fluxes in the NWP and climate models. The long-term flux series like those of CRA can now be taken as a reference for their evaluation. Figure 14 shows the difference between the modelled fluxes and the observed fluxes for both the sensible and the latent heat fluxes. It gives an example for only 1 year (2021), with monthly averages, so that interannual and intraseasonal variability are worn off here. The overestimation of the sensible and latent heat fluxes by the two models from April to September is consistent with what Couvreux et al. (2016) found during the BLLAST experiment in June 2011. One plausible explanation was related to the land use (with more forest than real land use in several grid points, especially in ARPEGE) and soil moisture. However, under specific conditions during BLLAST, which correspond to a heatwave and very small or negative surface fluxes, the models underestimated the fluxes. Here, in autumn and winter, we find, on average, an underestimation of the sensible heat flux by the models, while the latent heat flux remains generally overestimated. The former could be related to the underestimation of the 2 m temperature almost all year long (not
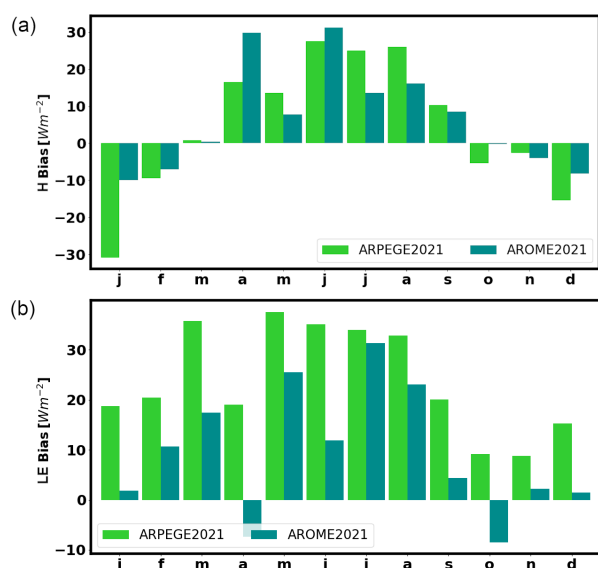
Figure 14. Difference between the monthly **(a)** sensible and **(b)** latent heat fluxes observed at 30 m at CRA and simulated by ARPEGE and AROME NWP models.

shown), with larger negative biases in winter and autumn, reaching down to $-2.5\,°C$, on average, in December 2021 in ARPEGE, for example. This reveals the difficulty of such comparisons when the environment itself (temperature, relative humidity, wind, radiation and clouds, soil conditions, etc.) may differ between the model and observations, leading to different surface heat fluxes. In this case, it is not possible to make conclusions regarding the capability of the models to correctly represent the surface fluxes.

This type of comparison is thus of clear interest as a first step for model evaluation, but is not sufficient to make conclusions regarding true model biases and their sources. One first needs to fully understand the representativity of the measured flux and the meaning of the modelled flux for a given grid point. It is, as a second step, important to consider an appropriate way to compare both together for model evaluation, which would be different compared to such a direct point-to-point comparison. This is the core question of the MOSAI project (Lohou et al., 2023). In its context, Zouzoua et al. (2024), for example, propose a new method for model evaluation based on supervised neural networks.

6.3.3 Validation of a regional climate model based on aerosol composition

A 1-year sensitivity study was performed at the European scale with the Regional Climate Model (RegCM, Filippo et al., 2012) over the year 2010. Aerosol radiative forcings and feedbacks are highly dependent on the physical, optical, and chemical properties of aerosols and on their spatial and temporal distributions. Aerosol sources, transport, and sink performances of RegCM were assessed for the year 2010

over the complex terrain of the Pyrenees thanks to the PDM aerosol dataset.

Simulated monthly mean aerosol concentrations were evaluated against in situ aerosol concentrations of elemental carbon (EC), organic carbon (OC), aerosol sulfate (SO_4^{2-}), calcium ion (Ca^{2+}), magnesium ion (Mg^{2+}), chlorine ion (Cl^-), and sodium ion (Na^+) from PDM. Ca^{2+} and Mg^{2+} are considered to be dust tracers, and Cl^- and Na^+ are considered to be sea salt (SSLT) tracers. Monthly means of PDM aerosol tracer concentrations were calculated from weekly filter samplings. The weekly sampling integrated volumes of air pumped continuously for 7 d. The chemical analyses performed on these filters were ion chromatography analysis for the inorganic fraction of aerosols (World Meteorological Organization Quality Assurance/Science Activity Centre (WMO QA/SAC) (http://www.qasac-americas.org/, last access: 16 October 2024, laboratory no. 700106) and thermo-optical analysis according to the IMPROVE protocol (Chow et al., 2007) for the organic fraction of aerosols for the year studied. The analytical errors were estimated to be 5 %.

In Fig. 15, monthly averages for 2010 are plotted, as well as the monthly averages over the period 2002–2018. Comparing these two trends allows the 2010 variation to be compared to an average variation over a 17-year dataset. The 2010 seasonal variation lies within 1 standard deviation around the multi-year average. Only the month of July 2010 shows an average of each chemical compound outside the multi-annual average and associated standard deviation, which is related to the fact that the number of samples contributing to the average is less important and represents specific episodes. The high standard deviations around the multi-annual mean of calcium and magnesium ions (Fig. 15b) show the occasional occurrence of intense dust episodes over PDM.

The BC and OC seasonal variabilities are well reproduced by the model as the modelled seasonal variations of BC and OC compounds are comparable to the seasonal variations of measured EC and OC. The model seems to reproduce well the temporal occurrence of regional-scale biomass burning and secondary organic aerosol during the summer period (Fig. 15a). Only the magnitudes of these annual trends are not comparable, with the model largely underestimating the concentrations. This is related to the overestimated dry deposition for carbonaceous aerosol parameterized in the model.

Modelled sulfate concentrations show a temporal evolution and an intensity of orders of magnitude comparable to those of sulfate measurements (Fig. 15c). Figure 15b shows that the model overestimates the dust aerosol concentrations all throughout the year with a large magnitude. Tsikerdekis et al. (2017) showed, through a sensitivity study, that RegCM overestimates dust emission fluxes. The seasonal variation seems to present little consistency with the measurements during the months of March and April. Concerning sea salt concentrations (Fig. 15d), the modelled concentrations show an annual variation that does not agree with the measurement of marine-influence tracers at PDM. This reveals again the
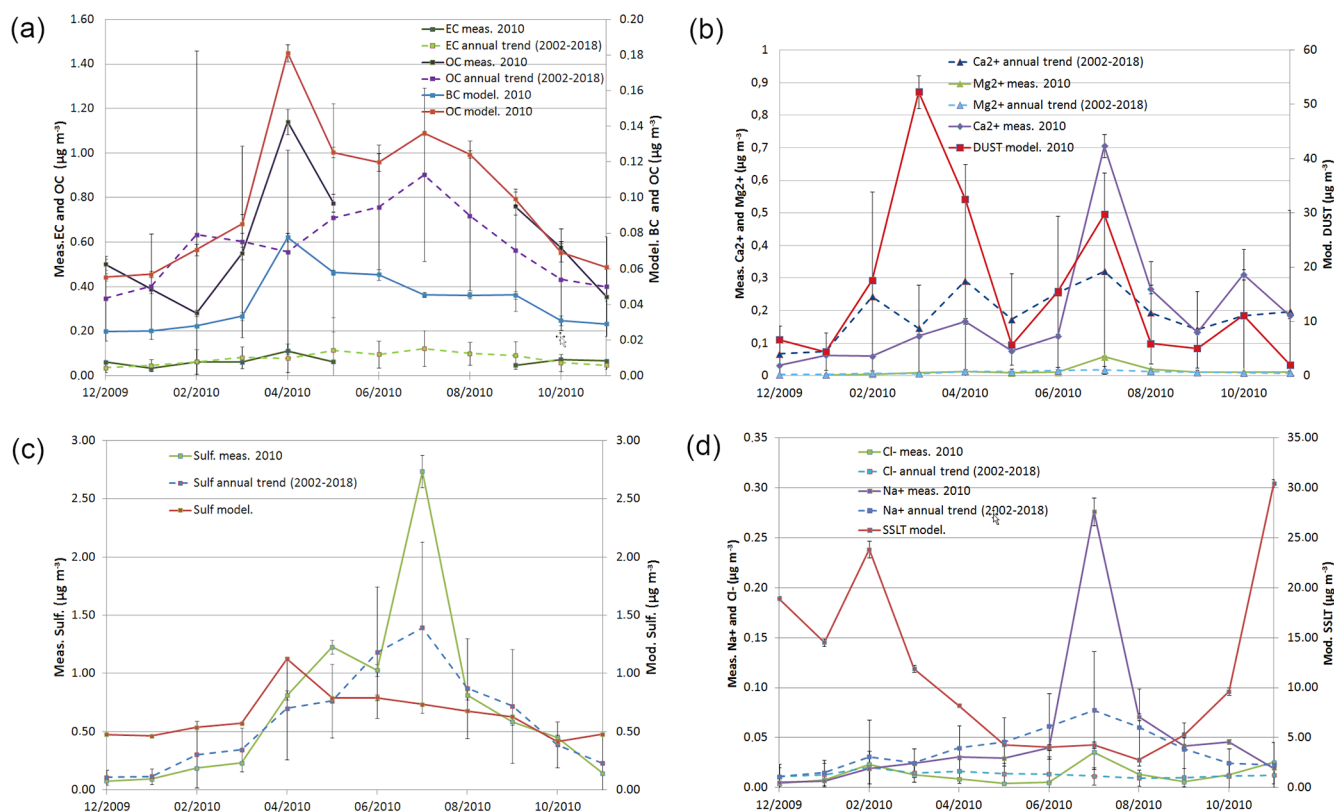
Figure 15. Annual trends of monthly mean mass concentrations ($\mu g\,m^{-3}$) of aerosol compounds modelled with RegCM in the Pyrenean region over the year 2010 with a horizontal spatial resolution of $35\,km \times 35\,km$ compared to monthly mean concentrations measured in situ at PDM. **(a)** Modelled BC and OC mixing ratios with measured EC and OC. **(b)** Modelled dust mixing ratio with Ca^{2+} and Mg^{2+} measured as main tracers of dust influence. **(c)** Modelled SO_4^{2-} mixing ratio with measured sulfate concentrations. **(d)** Modelled SSLT mixing ratio with Na^+ and Cl^- measured concentrations as main tracers of marine influence.

problem of overestimation of the marine aerosol sources parameterized in the model according to the intensity of the wind fields in the cyclonic season over the oceanic area.

7 Conclusions

To conclude, we have shown that a broad spectrum of scientific questions and applications can be addressed based on the long-term dataset collected at P2OA due to the rich set of instruments used for meteorological dynamics, atmospheric composition, or electricity. Emphasis is given to specific areas of expertise, such as atmospheric boundary layer dynamics, trace gas transport, aerosol chemical and physical properties, or transient luminous events. Most continuously operated instruments are connected to a French or international network for weather forecasting services, climate and air quality monitoring, or atmospheric-process studies.

From the point of view of air composition, the location of P2OA near the Atlantic Ocean makes it weakly influenced by human activity on continental Europe. Further, its implementation near the Pyrenees makes it specific for complex terrain studies. The coupling of the high-altitude site at PDM

and the plain site at CRA favours the analysis of orographically forced regimes and their impact on the exchange and transport of trace species.

With such a set of instruments and the capability of its infrastructure (lodging, workshops, meeting and conference rooms, etc.), P2OA is also a well-equipped hosting facility. CRA is especially suited to operate light RPAS and balloons, and PDM is suited to experiments at high altitudes. However, beyond these specificities, a broad spectrum of instrumental tests or field campaigns took place at P2OA. P2OA is also a favourable and recognized place for educational training in atmospheric research: 8 to 10 undergraduate- or Masters-level training sessions are organized yearly based on micro field campaigns (radiosoundings, surface energy balance stations, etc.) and the use of the permanent instruments.

In the context of the main science topics addressed at P2OA and illustrated before, the following perspectives regarding new instrumentation are foreseen:

– A new high-resolution Doppler lidar should be installed at the CRA site by the end of 2024, complementary to all other devices for the description of the atmospheric boundary layer dynamics. Its fine temporal and spa-

tial resolutions should give more turbulence statistics in clear air and should open new horizons for the turbulence retrieval observational techniques.

- As a coming contribution to the European ACTRIS infrastructure, two monitoring systems of atmospheric short-lived reactive gases will be installed at PDM in 2024: a proton transfer reaction–time-of-flight mass spectrometer for measuring a selection of volatile organic compounds and a NO/NO_2 monitoring system. These instruments will complement existing aerosol and gas measurements at PDM as the targeted species are chemical precursors of ozone and secondary aerosols. They will also allow for a much better characterization of emission sources affecting the sampled air masses: biomass burning (from agriculture or forest fires), anthropogenic benzene sources, oceanic influence, etc.

Appendix A: Instrumentation of the 60 m tower

Table A1. Instruments installed on the 60 m tower of P2OA-CRA, listed by height, with corresponding measured variables and sampling frequency.

Height	Sensor	Main variable(s)	Frequency
2 m	Barometer	Pressure	0.1 Hz
	Rain gauge	Rainfall	0.1 Hz
	HMP45	Temperature, humidity	0.1 Hz
	Flux plates (3)	Ground heat flux	0.1 Hz
	HMP45	Temperature, humidity	0.1 Hz
	Wind vane	Wind direction	0.1 Hz
	Wind anemometer	Wind speed	0.1 Hz
30 m	HMP45	Temperature, humidity	1 Hz
	Sonic anemometer CSAT3	3D wind, virtual temperature	10 Hz
	LI-COR LI7500	Water vapour and CO_2 concentration	10 Hz
45 m	HMP45	Temperature, humidity	1 Hz
	Sonic anemometer GILL	3D wind, virtual temperature	10 Hz
	Wind vane	Wind direction	0.1 Hz
	Wind anemometer	Wind speed	0.1 Hz
60 m	Radiometer CNR1	Up. and down. SW and LW radiation	1 Hz
	HMP45	Temperature, humidity	1 Hz
	Sonic anemometer CSAT3	3D wind, virtual temperature	10 Hz

Appendix B: Glossary of acronyms

Table B1. List of acronyms or (in italic) names for research infrastructures, networks, databases, or algorithms.

Acronym	Definition	URL (last access for all URLs cited in this table is: 16 October 2024 if not stated otherwise)
ACTRIS	Aerosol, Clouds and Trace gases Research Infrastructure	https://www.actris.eu/
AERIS	*Data and Services for the Atmosphere*	https://www.aeris-data.fr/en/welcome-2/
ARM	Atmospheric radiation measurement	https://www.arm.gov/
AROME	*Météo-France small-scale numerical prediction model*	https://www.umr-cnrm.fr/spip.php?article120&lang=en
ARPEGE	*Météo-France global numerical weather prediction model*	http://www.umr-cnrm.fr/spip.php?article121&lang=en
EC, BC, and OC	Elemental carbon, black carbon, and organic carbon	
CALOTRITON	*Algorithm for CBL depth retrieval from radar wind profiler*	
CBL	Convective boundary layer	
CNRS	Centre national de la recherche scientifique	https://www.cnrs.fr/en
CO-PDD	Cézeaux-Aulnat-Opme-Puy De Dôme	https://opgc.uca.fr/co-pdd
DESMAN	*Algorithm for wind vector retrieval from radar wind profiler data*	
ELIFAN	*Algorithm for cloud fraction estimation from sky imagers*	
EUMETNET	European Meteorological Network	https://www.eumetnet.eu/
EUSAAR	*Thermo-optical protocol for elemental and organic carbon retrieval*	
E-Profile	EUMETNET profile	https://www.eumetnet.eu/activities/observations-programme/current-activities/e-profile/
GAW	Global Atmospheric Watch	https://community.wmo.int/en/activity-areas/gaw
GMOS	Global Mercury Observation System	https://gmos.aeris-data.fr/
GOS^{4}M	Global Observation System for Mercury	http://www.gos4m.org/
ICOS	Integrated Carbon Observation System	https://www.icos-cp.eu/
iGOS^{4}M	Online database of mercury stable isotopes	http://igos4m.com/
INSU	National Institute of Universe Sciences	https://www.insu.cnrs.fr/en
IRSN	Institute for Radioprotection and Nuclear Safety	https://en.irsn.fr/
Linet	Lightning detection network	https://www.nowcast.de/en/solutions/linet-systems/
NDACC	Network for the Detection of Atmospheric Composition Change	Lightning detection network
NWP	Numerical weather prediction	
OHP	Observatory of Haute Provence	https://ohp-geo.obs-hp.fr/ (last access: June 2024)
OPAR	Observatory of Atmospheric Physics at La Réunion	https://opar.univ-reunion.fr/ (last access: 17 October 2024)
P2OA	Pyrenean Platform for Observation of the Atmosphere	https://p2oa.aeris-data.fr/
ReNAG	GNSS national network	https://www.osug.fr/missions/observation/terre-solide/renag-gnss-permanent/
ReOBS	*New approach to synthesize long-term multi-variable dataset*	https://reobs.aeris-data.fr/

Table B1. Continued.

Acronym	Definition	URL (last access for all URLs cited in this table is: 16 October 2024 if not stated otherwise)
Ro5	Ring of five	https://www.iur-uir.org/en/pro/task-groups/id-22-ring-of-five-task-group
RPAS	Remotely piloted aeroplane system	
SIRTA	Instrumented Site for Remote Sensing Atmospheric Research	https://sirta.ipsl.fr/fr/home-fr-2/
StatIC	InfoClimat Stations network	https://www.infoclimat.fr/stations/static.php
STRATFinder	*Algorithm for CBL depth retrieval from lidar and ceilometer*	https://gitlab.in2p3.fr/ipsl/sirta/mld/stratfinder/stratfinder
TELERAY	*Gamma dose rate alert national network*	https://teleray.irsn.fr/#mappage
TLE	Transient luminous event	
TOPROF	Towards operational ground-based profiling	http://www.toprof.imaa.cnr.it/
UFOCapture	Time Shifted Motion Capture Software for high-definition images	https://sonotaco.com/soft/e_index.html
UHF	Ultra-high frequency	
VHF	Very high frequency	

Review statement. This paper was edited by Pinhua Xie and reviewed by three anonymous referees.

References

Alaoui-Sosse, S., Durand, P., Medina, P., Pastor, P., Lothon, M., and Cernov, I.: OVLI-TA: An Unmanned Aerial System for Measuring Profiles and Turbulence in the Atmospheric Boundary Layer, Sensors, 19, 581, https://doi.org/10.3390/s19030581, 2019.

Alaoui-Sosse, S., Durand, P., Medina, P., Pastor, P., Gavart, M., and Pizziol, S.: BOREAL-A Fixed-Wing Unmanned Aerial System for the Measurement of Wind and Turbulence in the Atmospheric Boundary Layer, J. Atmos. Ocean. Tech., 39, 387–402, 2022.

Allen, S., Allen, D., Baladima, F., Phoenix, V., Thomas, J., Le Roux, G., and Sonke, J.: Evidence of free tropospheric and long-range transport of microplastic at Pic du Midi Observatory, Nat. Commun., 12, 7242, https://doi.org/10.1038/s41467-021-27454-7, 2021.

Amestoy, J.: Etude de l'influence des facteurs environnementaux sur la spectrométrie gamma aéroportée et application à la surveillance environnementale de sites, PhD thesis, Université Toulouse III, https://theses.hal.science/tel-03515339 (last access: 16 October 2024), 2021.

Amestoy, J., Meslin, P. Y., Richon, P., Delpuech, A., Derrien, S., Raynal, H., Pique, E., Baratoux, D., Chotard, P., Van Beek, P., Souhaut, M., and Zambardi, T.: Effects of environmental factors on the monitoring of environmental radioactivity by airborne gamma-ray spectrometry, J. Environ. Radioactiv., 237, 106695, https://doi.org/10.1016/j.jenvrad.2021.106695, 2021.

Ammoura, L., Xueref-Remy, I., Vogel, F., Gros, V., Baudic, A., Bonsang, B., Delmotte, M., Té, Y., and Chevallier, F.: Exploiting stagnant conditions to derive robust emission ratio estimates for CO_2, CO and volatile organic compounds in Paris, Atmos. Chem. Phys., 16, 15653–15664, https://doi.org/10.5194/acp-16-15653-2016, 2016.

Argentini, S., Viola, A., Sempreviva, A., and Petenko, I.: Summer boundary-layer height at the plateau site of Dome'C, antarctica, Bound.-Lay. Meteorol., 115, 409–422, https://doi.org/10.1007/s10546-004-5643-6, 2005.

Arnone, E., Bór, J., Chanrion, O., Barta, V., Dietrich, S., Enell, C. F., Farges, T., Füllekrug, M., Kero, A., Labanti, R., Mäkelä, A., Mezuman, K., Odzimek, A., Popek, M., Prevedelli, M., Ridolfi, M., Soula, S., Valeri, D., van der Velde, O., Yair, Y., Zanotti, F., Zoladek, P., and Neubert, T.: Climatology of Transient Luminous Events and Lightning Observed Above Europe and the Mediterranean Sea, Surv. Geophys., 41, 167–199, https://doi.org/10.1007/s10712-019-09573-5, 2020.

Bamberger, I., Oney, B., Brunner, D., Henne, S., Leuenberger, M., Buchmann, N., and Eugster, W.: Observations of Atmospheric Methane and Carbon Dioxide Mixing Ratios: Tall-Tower or Mountain-Top Stations?, Bound.-Lay. Meteorol., 164, 135–159, https://doi.org/10.1007/s10546-017-0236-3, 2017.

Baray, J.-L., Courcoux, Y., Keckhut, P., Portafaix, T., Tulet, P., Cammas, J.-P., Hauchecorne, A., Godin Beekmann, S., De Mazière, M., Hermans, C., Desmet, F., Sellegri, K., Colomb, A., Ramonet, M., Sciare, J., Vuillemin, C., Hoareau, C., Dionisi, D., Duflot, V., Vérèmes, H., Porteneuve, J., Gabarrot, F., Gaudo, T., Metzger, J.-M., Payen, G., Leclair de Bellevue, J., Barthe, C., Posny, F., Ricaud, P., Abchiche, A., and Delmas, R.: Maïdo observatory: a new high-altitude station facility at Reunion Island (21° S, 55° E) for long-term atmospheric remote sensing and in situ measurements, Atmos. Meas. Tech., 6, 2865–2877, https://doi.org/10.5194/amt-6-2865-2013, 2013.

Baray, J.-L., Bah, A., Cacault, P., Sellegri, K., Pichon, J.-M., Deguillaume, L., Montoux, N., Noel, V., Seze, G., Gabarrot, F., Payen, G., and Duflot, V.: Cloud Occurrence Frequency at Puy de Dôme (France) Deduced from an Automatic Camera Image Analysis: Method, Validation, and Comparisons with Larger Scale Parameters, Atmosphere, 10, 808, https://doi.org/10.3390/atmos10120808, 2019.

Baray, J.-L., Deguillaume, L., Colomb, A., Sellegri, K., Freney, E., Rose, C., Van Baelen, J., Pichon, J.-M., Picard, D., Fréville, P., Bouvier, L., Ribeiro, M., Amato, P., Banson, S., Bianco, A., Borbon, A., Bourcier, L., Bras, Y., Brigante, M., Cacault, P., Chauvigné, A., Charbouillot, T., Chaumerliac, N., Delort, A.-M., Delmotte, M., Dupuy, R., Farah, A., Febvre, G., Flossmann, A., Gourbeyre, C., Hervier, C., Hervo, M., Huret, N., Joly, M., Kazan, V., Lopez, M., Mailhot, G., Marinoni, A., Masson, O., Montoux, N., Parazols, M., Peyrin, F., Pointin, Y., Ramonet, M., Rocco, M., Sancelme, M., Sauvage, S., Schmidt, M., Tison, E., Vaïtilingom, M., Villani, P., Wang, M., Yver-Kwok, C., and Laj, P.: Cézeaux-Aulnat-Opme-Puy De Dôme: a multi-site for the long-term survey of the tropospheric composition and climate change, Atmos. Meas. Tech., 13, 3413–3445, https://doi.org/10.5194/amt-13-3413-2020, 2020.

Båserud, L., Reuder, J., Jonassen, M. O., Kral, S. T., Paskyabi, M. B., and Lothon, M.: Proof of concept for turbulence measurements with the RPAS SUMO during the BLLAST campaign, Atmos. Meas. Tech., 9, 4901–4913, https://doi.org/10.5194/amt-9-4901-2016, 2016.

Båserud, L., Reuder, J., Jonassen, M. O., Bonin, T. A., Chilson, P. B., Jiménez, M. A., and Durand, P.: Potential and Limitations in Estimating Sensible-Heat-Flux Profiles from Consecutive Temperature Profiles Using Remotely-Piloted Aircraft Systems, Bound.-Lay. Meteorol., 174, 145–177, 2020.

Bergamaschi, P., Colomb, A., De Mazière, M., Emmenegger, L., Kubistin, D., Lehner, I., Lehtinen, K., Lund Myhre, C., Marek, M., Platt, S., Plaß-Dülmer, C., Apadula, F., Arnold, S., Blanc, P.-E., Brunner, D., Chen, H., Chmura, A., Chmura, L., Conil, S., Couret, C., Cristofanelli, P., Di Iorio enea, T., Forster, G., Frumau, A., Gerbig, C., Gheusi, F., Hammer, S., Haszpra, L., Hatakka, J., Heliasz, M., Henne, S., Hensen, A., Hoheisel, A., Kneuer, T., Larmanou, E., Laurila, T., Leskinen, A., Leuenberger, M., Levin, I., Lindauer, M., Mammarella, I., Manca, G., Manning, A., Marklund, P., Martin, D., Meinhardt, F., Müller-Williams, J., Noe, S., Nęcki, J., O'Doherty, S., Ottosson-Löfvenius, M., Philippon, C., Piacentino, S., Pitt, J., Ramonet, M., Rivas-Soriano, P., Scheeren, B., Schumacher, M., Sha, M.

K., Smith, P., Spain, G., Steinbacher, M., Sørensen, L., Vermeulen, A., Vítková, G., Xueref-Remy, I., di Sarra, A., Conen, F., Kazan, V., Roulet, Y.-A., Biermann, T., Delmotte, M., Heltai, D., Hermansen, O., Komínková, K., Laurent, O., Levula, J., Lopez, M. andLunder, C., Morguí, J.-A., Pichon, J.-M., Schmidt, M., Sferlazzo, D., Stanley, K., Trisolino, P., and Zazzeri, G.: European Obspack compilation of atmospheric carbon dioxide data from ICOS and non-ICOS European stations for the period 1972–2024, obspack_co2_466_GVeu_v10_20240729, https://doi.org/10.18160/X450-GTAY, 2024a.

Bergamaschi, P., Colomb, A., De Mazière, M., Emmenegger, L., Kubistin, D., Lehner, I., Lehtinen, K., Lund Myhre, C., Marek, M., Platt, S., Plaß-Dülmer, C., Apadula, F., Arnold, S., Blanc, P.-E., Brunner, D., Chen, H., Chmura, A., Chmura, L., Conil, S., Couret, C., Cristofanelli, P., Di Iorio enea, T., Forster, G., Frumau, A., Gerbig, C., Gheusi, F., Hammer, S., Haszpra, L., Hatakka, J., Heliasz, M., Henne, S., Hensen, A., Hoheisel, A., Kneuer, T., Larmanou, E., Laurila, T., Leskinen, A., Leuenberger, M., Levin, I., Lindauer, M., Mammarella, I., Manca, G., Manning, A., Marklund, P., Martin, D., Meinhardt, F., Müller-Williams, J., Noe, S., Nęcki, J., O'Doherty, S., Ottosson-Löfvenius, M., Philippon, C., Piacentino, S., Pitt, J., Ramonet, M., Rivas-Soriano, P., Scheeren, B., Schumacher, M., Sha, M. K., Smith, P., Spain, G., Steinbacher, M., Sørensen, L., Vermeulen, A., Vítková, G., Xueref-Remy, I., di Sarra, A., Conen, F., Kazan, V., Roulet, Y.-A., Biermann, T., Delmotte, M., Heltai, D., Hermansen, O., Komínková, K., Laurent, O., Levula, J., Lopez, M., Lunder, C., Morguí, J.-A., Pichon, J.-M., Schmidt, M., Sferlazzo, D., Stanley, K., Trisolino, P., and Zazzeri, G.: European Obspack compilation of atmospheric methane data from ICOS and non-ICOS European stations for the period 1984–2024, obspack_ch4_466_GVeu_v10_20240729, ICOS [dataset], https://doi.org/10.18160/PAWA-B2Y4, 2024b.

Blay-Carreras, E., Pardyjak, E. R., Pino, D., Alexander, D. C., Lohou, F., and Lothon, M.: Countergradient heat flux observations during the evening transition period, Atmos. Chem. Phys., 14, 9077–9085, https://doi.org/10.5194/acp-14-9077-2014, 2014a.

Blay-Carreras, E., Pino, D., Vilà-Guerau de Arellano, J., van de Boer, A., De Coster, O., Darbieu, C., Hartogensis, O., Lohou, F., Lothon, M., and Pietersen, H.: Role of the residual layer and large-scale subsidence on the development and evolution of the convective boundary layer, Atmos. Chem. Phys., 14, 4515–4530, https://doi.org/10.5194/acp-14-4515-2014, 2014b.

Blay-Carreras, E., Pardyjak, E. R., Pino, D., Hoch, S. W., Cuxart, J., Martínez, D., and Reuder, J.: Lifted temperature minimum during the atmospheric evening transition, Atmos. Chem. Phys., 15, 6981–6991, https://doi.org/10.5194/acp-15-6981-2015, 2015.

Boehm, J., Werl, B., and Schuh, H.: Troposphere mapping functions for GPS and very long baseline interferometry from European Centre for Medium-Range Weather Forecasts operational analysis data, J. Geophys. Res., 111, B02406, https://doi.org/10.1029/2005JB003629, 2006.

Bosser, P. and Bock, O.: IWV retrieval from ground GNSS receivers during NAWDEX, Adv. Geosci., 55, 13–22, https://doi.org/10.5194/adgeo-55-13-2021, 2021.

Bosveld, F., Baas, P., Beljaars, A., Holtslag, A. A. M., Vilà-Guerau de Arellano, J., and van de Wiel, B. J. H.: Fifty Years of Atmospheric Boundary-Layer Research at Cabauw Serving Weather,

Air Quality and Climate, Bound.-Lay. Meteorol., 177, 583–612, https://doi.org/10.1007/s10546-020-00541-w, 2020.

Bou-Zeid, E., Anderson, W., Katul, G. G., and Mahrt, L.: The Persistent Challenge of Surface Heterogeneity in Boundary-Layer Meteorology: A Review, Bound.-Lay. Meteorol., 177, 227–245, 2020.

Bougeault, P., Clar, A., Bénech, B., Carissimo, B., Pelon, J., and Richard, E.: Momentum budget over the Pyrenees – The PYREX experiment, B. Am. Meteorol. Soc., 71, 806–818, 1990.

Browning, K. A. and Wexler, R.: The determination of kinematic properties of a wind field using Doppler radar, J. Appl. Meteorol. Clim., 7, 105–113, 1968.

Bücher, A. and Dessens, J.: Secular trend of surface temperature at an elevated observatory in the Pyrenees, J. Climate, 4, 859–868, 1991.

Calmer, R., Roberts, G. C., Preissler, J., Sanchez, K. J., Derrien, S., and O'Dowd, C.: Vertical wind velocity measurements using a five-hole probe with remotely piloted aircraft to study aerosol–cloud interactions, Atmos. Meas. Tech., 11, 2583–2599, https://doi.org/10.5194/amt-11-2583-2018, 2018.

Calmer, R., Roberts, G. C., Sanchez, K. J., Sciare, J., Sellegri, K., Picard, D., Vrekoussis, M., and Pikridas, M.: Aerosol–cloud closure study on cloud optical properties using remotely piloted aircraft measurements during a BACCHUS field campaign in Cyprus, Atmos. Chem. Phys., 19, 13989–14007, https://doi.org/10.5194/acp-19-13989-2019, 2019.

Campistron, B., Long, A. B., and Hugins, A. W.: A methof of retrieving turbulence parameters from volume processing of single-Doppler radar measurements, J. Atmos. Ocean. Tech., 8, 491–505, 1991.

Campistron, B., Point, Y., Lohou, F., and Pages, J.-P.: Aspect sensitivity of VHF radar echoes observed in the middle and upper troposphere during the passage of a cut-off low, Radio Sci., 34, 667–679, 1999.

Canut, G., Couvreux, F., Lothon, M., Legain, D., Piguet, B., Lampert, A., Maurel, W., and Moulin, E.: Turbulence fluxes and variances measured with a sonic anemometer mounted on a tethered balloon, Atmos. Meas. Tech., 9, 4375–4386, https://doi.org/10.5194/amt-9-4375-2016, 2016.

Canut, G., Calvet, J. C., Maurel, W., and Paci, A.: Seven years (2012–2018) of continuous observation of the surface energy budget and of soil moisture and temperature profiles in a peri-urban area, EMS Annual Meeting, 9–13 September 2019, Lyngby, Denmark, EMS2019-687-1, 2019.

Cavalli, F., Viana, M., Yttri, K. E., Genberg, J., and Putaud, J.-P.: Toward a standardised thermal-optical protocol for measuring atmospheric organic and elemental carbon: the EUSAAR protocol, Atmos. Meas. Tech., 3, 79–89, https://doi.org/10.5194/amt-3-79-2010, 2010.

Chambers, S. D., Zahorowski, W., Williams, A. G., Crawford, J., and Griffiths, A. D.: Identifying tropospheric baseline air masses at Mauna Loa Observatory between 2004 and 2010 using Radon-222 and back trajectories, J. Geophys. Res.-Atmos., 118, 992–1004, https://doi.org/10.1029/2012JD018212, 2013.

Chambers, S. D., Williams, A. G., Conen, F., Griffiths, A. D., Reimann, S., Steinbacher, M., Krummel, P. B., Steele, L. P., van der Schoot, M. V., Galbally, I. E., Molloy, S. B., and Barnes, J. E.: Towards a Universal "Baseline" Characterisation of Air Masses for High- and Low-Altitude Observing Sta-

tions Using Radon-222, Aerosol Air Qual. Res., 16, 885–899, https://doi.org/10.4209/aaqr.2015.06.0391, 2016.

Chevalier, A., Gheusi, F., Delmas, R., Ordóñez, C., Sarrat, C., Zbinden, R., Thouret, V., Athier, G., and Cousin, J.-M.: Influence of altitude on ozone levels and variability in the lower troposphere: a ground-based study for western Europe over the period 2001–2004, Atmos. Chem. Phys., 7, 4311–4326, https://doi.org/10.5194/acp-7-4311-2007, 2007.

Chiriaco, M., Dupont, J.-C., Bastin, S., Badosa, J., Lopez, J., Haeffelin, M., Chepfer, H., and Guzman, R.: ReOBS: a new approach to synthesize long-term multi-variable dataset and application to the SIRTA supersite, Earth Syst. Sci. Data, 10, 919–940, https://doi.org/10.5194/essd-10-919-2018, 2018.

Chow, J. C., Watson, J. G., Antony Chen, L. W., Oliver Chang, M. C., Robinson, N. F., Trimble, D., and Kohl, S.: The IMPROVE_A Temperature Protocol for Thermal/Optical Carbon Analysis: Maintaining Consistency with a Long-Term Database, J. Air Waste Manage., 57, 1014–1023, https://doi.org/10.3155/1047-3289.57.9.1014, 2007.

Collaud Coen, M., Weingartner, E., Furger, M., Nyeki, S., Prévôt, A. S. H., Steinbacher, M., and Baltensperger, U.: Aerosol climatology and planetary boundary influence at the Jungfraujoch analyzed by synoptic weather types, Atmos. Chem. Phys., 11, 5931–5944, https://doi.org/10.5194/acp-11-5931-2011, 2011.

Collaud Coen, M., Andrews, E., Aliaga, D., Andrade, M., Angelov, H., Bukowiecki, N., Ealo, M., Fialho, P., Flentje, H., Hallar, A. G., Hooda, R., Kalapov, I., Krejci, R., Lin, N.-H., Marinoni, A., Ming, J., Nguyen, N. A., Pandolfi, M., Pont, V., Ries, L., Rodríguez, S., Schauer, G., Sellegri, K., Sharma, S., Sun, J., Tunved, P., Velasquez, P., and Ruffieux, D.: Identification of topographic features influencing aerosol observations at high altitude stations, Atmos. Chem. Phys., 18, 12289–12313, https://doi.org/10.5194/acp-18-12289-2018, 2018.

Courtier, P. and Geleyn, J.-F.: The AROME-France Convective-Scale Operational Model, Q. J. Roy. Meteor. Soc., 114, 1321–1346, 1988.

Couvreux, F., Bazile, E., Canut, G., Seity, Y., Lothon, M., Lohou, F., Guichard, F., and Nilsson, E.: Boundary-layer turbulent processes and mesoscale variability represented by numerical weather prediction models during the BLLAST campaign, Atmos. Chem. Phys., 16, 8983–9002, https://doi.org/10.5194/acp-16-8983-2016, 2016.

Cristofanelli, P., Fratticioli, C., Hazan, L., Chariot, M., Couret, C., Gazetas, O., Kubistin, D., Laitinen, A., Leskinen, A., Laurila, T., Lindauer, M., Manca, G., Ramonet, M., Trisolino, P., and Steinbacher, M.: Identification of spikes in continuous ground-based in situ time series of CO_2, CH_4 and CO: an extended experiment within the European ICOS Atmosphere network, Atmos. Meas. Tech., 16, 5977–5994, https://doi.org/10.5194/amt-16-5977-2023, 2023.

Cuxart, J., Wrenger, B., Martínez-Villagrasa, D., Reuder, J., Jonassen, M. O., Jiménez, M. A., Lothon, M., Lohou, F., Hartogensis, O., Dünnermann, J., Conangla, L., and Garai, A.: Estimation of the advection effects induced by surface heterogeneities in the surface energy budget, Atmos. Chem. Phys., 16, 9489–9504, https://doi.org/10.5194/acp-16-9489-2016, 2016.

Darbieu, C., Lohou, F., Lothon, M., Vilà-Guerau de Arellano, J., Couvreux, F., Durand, P., Pino, D., Patton, E. G., Nilsson, E., Blay-Carreras, E., and Gioli, B.: Turbulence vertical structure of the boundary layer during the afternoon transition, Atmos. Chem. Phys., 15, 10071–10086, https://doi.org/10.5194/acp-15-10071-2015, 2015.

Dessens, J. and Bücher, A.: Changes in minimum and maximum temperature at the Pic du Midi in relation with humidity and cloudiness, 1882–1984, Atmos. Res., 37, 147–162, 1995.

De Wekker, S.: Observational and Numerical Evidence of Depressed Convective Boundary Layer Heights near a Mountain Base, J. Appl. Meteorol. Clim., 47, 1017–1026, https://doi.org/10.1175/2007JAMC1651.1, 2008.

El Guernaoui, O., Reuder, J., Esau, I., Wolf, T., and Maronga, B.: Scaling the Decay of Turbulence Kinetic Energy in the Free-Convective Boundary Layer, Bound.-Lay. Meteorol., 173, 79–97, 2016.

Elvidge, A. D. and Renfrew, I. A.: The causes of foehn warming in the lee of mountains, B. Am. Meteorol. Soc., 97, 455–466, https://doi.org/10.1175/BAMS-D-14-00194.1, 2016.

El Yazidi, A., Ramonet, M., Ciais, P., Broquet, G., Pison, I., Abbaris, A., Brunner, D., Conil, S., Delmotte, M., Gheusi, F., Guerin, F., Hazan, L., Kachroudi, N., Kouvarakis, G., Mihalopoulos, N., Rivier, L., and Serça, D.: Identification of spikes associated with local sources in continuous time series of atmospheric CO, CO_2 and CH_4, Atmos. Meas. Tech., 11, 1599–1614, https://doi.org/10.5194/amt-11-1599-2018, 2018.

Enrico, M., Le Roux, G., Maruszczak, N., Heimbürger, L.-E., Claustres, A., Fu, X., Sun, R., and Sonke, J.: Atmospheric mercury transfer to peat bogs dominated by gaseous elemental mercury dry deposition, Environ. Sci. Technol., 50, 2405–2412, https://doi.org/10.1021/acs.est.5b06058, 2016.

Evrard, O., Van Beek, P., Gateuille, D., Pont, V., Lefèvre, I., Lansard, B., and Bonté, P.: Evidence of the radioactive fallout in France due to the Fukushima nuclear accident, J. Environ. Radioactiv., 114, 54–60, https://doi.org/10.1016/j.jenvrad.2012.01.024, 2012.

Filippo, G., Coppola, E., Solmon, F., Mariotti, L., Sylla, M. B., Bi, X., and Elguindi, N., Diro, G. T., Nair, V., Giuliani, G., Turuncoglu, U. U., Cozzini, S., Güttler, I., O'Brien, T. A., Tawfik, A. B., Shalaby, A., Zakey, A. S., Steiner, A. L., Stordal, F., Sloan, L. C., and Brankovic, C.: RegCM4: model description and preliminary tests over multiple CORDEX domains, Clim. Res., 52, 7–29, https://doi.org/10.3354/cr01018, 2012.

Friedlingstein, P., O'Sullivan, M., Jones, M. W., Andrew, R. M., Bakker, D. C. E., Hauck, J., Landschützer, P., Le Quéré, C., Luijkx, I. T., Peters, G. P., Peters, W., Pongratz, J., Schwingshackl, C., Sitch, S., Canadell, J. G., Ciais, P., Jackson, R. B., Alin, S. R., Anthoni, P., Barbero, L., Bates, N. R., Becker, M., Bellouin, N., Decharme, B., Bopp, L., Brasika, I. B. M., Cadule, P., Chamberlain, M. A., Chandra, N., Chau, T.-T.-T., Chevallier, F., Chini, L. P., Cronin, M., Dou, X., Enyo, K., Evans, W., Falk, S., Feely, R. A., Feng, L., Ford, D. J., Gasser, T., Ghattas, J., Gkritzalis, T., Grassi, G., Gregor, L., Gruber, N., Gürses, Ö., Harris, I., Hefner, M., Heinke, J., Houghton, R. A., Hurtt, G. C., Iida, Y., Ilyina, T., Jacobson, A. R., Jain, A., Jarníková, T., Jersild, A., Jiang, F., Jin, Z., Joos, F., Kato, E., Keeling, R. F., Kennedy, D., Klein Goldewijk, K., Knauer, J., Korsbakken, J. I., Körtzinger, A., Lan, X., Lefèvre, N., Li, H., Liu, J., Liu, Z., Ma, L., Marland, G., Mayot, N., McGuire, P. C., McKinley, G. A., Meyer, G., Morgan, E. J., Munro, D. R., Nakaoka, S.-I., Niwa, Y., O'Brien, K. M., Olsen, A., Omar, A. M., Ono, T., Paulsen, M., Pierrot, D.,

Pocock, K., Poulter, B., Powis, C. M., Rehder, G., Resplandy, L., Robertson, E., Rödenbeck, C., Rosan, T. M., Schwinger, J., Séférian, R., Smallman, T. L., Smith, S. M., Sospedra-Alfonso, R., Sun, Q., Sutton, A. J., Sweeney, C., Takao, S., Tans, P. P., Tian, H., Tilbrook, B., Tsujino, H., Tubiello, F., van der Werf, G. R., van Ooijen, E., Wanninkhof, R., Watanabe, M., Wimart-Rousseau, C., Yang, D., Yang, X., Yuan, W., Yue, X., Zaehle, S., Zeng, J., and Zheng, B.: Global Carbon Budget 2023, Earth Syst. Sci. Data, 15, 5301–5369, https://doi.org/10.5194/essd-15-5301-2023, 2023.

Fu, X., Maruszczak, N., Heimbürger, L.-E., Sauvage, B., Gheusi, F., Prestbo, E. M., and Sonke, J. E.: Atmospheric mercury speciation dynamics at the high-altitude Pic du Midi Observatory, southern France, Atmos. Chem. Phys., 16, 5623–5639, https://doi.org/10.5194/acp-16-5623-2016, 2016a.

Fu, X., Maruszczak, N., Wang, X., Gheusi, F., and Sonke, J.: The isotopic composition of total gaseous mercury in the free troposphere of the Pic du Midi Observatory (2877 m a.s.l, France, Environ. Sci. Technol., 50, 5641–5650, https://doi.org/10.1021/acs.est.6b00033, 2016b.

Fu, X., Jiskra, M., Yang, X., Maruszczak, N., Enrico, M., Chmeleff, J., Heimbürger-Boavida, L.-E., Gheusi, F., and Sonke, J.: Mass-Independent Fractionation of Even and Odd Mercury Isotopes during Atmospheric Mercury Redox Reactions, Environ. Sci. Technol., 55, 10164–10174, https://doi.org/10.1021/acs.est.1c02568, 2021.

Füllekrug, M., Mareev, E. A., and Rycroft, M. J. (Eds.): Sprites, elves and intense lightning discharges, in: NATO Science Series II: Mathematics, physics and chemistry, Springer, Berlin, Vol. 225, https://doi.org/10.1007/1-4020-4629-4, 2006.

Garcelon, L., Brana, S., Didez, J., and Ameye, F.: StatIC : un réseau d'observation au service d'une information de proximité et de vulgarisation scientifique, La Météorologie, 122, 37–46, https://doi.org/10.37053/lameteorologie-2023-0071, 2023.

GAW: Guidelines for the measurement of atmospheric carbon monoxide - GAW report no. 192, Tech. rep., World Meteorological Organization (WMO), https://library.wmo.int/records/item/32181-guidelines-for-the-measurement-of-atmosphericcarbon-monoxide (last access: 17 October 2024), 2010.

GAW: Guidelines for the measurement of atmospheric carbon monoxide - GAW report no. 209, Tech. rep., World Meteorological Organization (WMO), https://community.wmo.int/en/bookstore/guidelines-continuous-measurements-ozone-troposphere (last access: 17 October 2024), 2013.

Gheusi, F. and Lothon, M.: P2OA Data Catalogue, AERIS, https://doi.org/10.25326/SJP8-TF88, 2024.

Gheusi, F., Ravetta, F., Delbarre, H., Tsamalis, C., Chevalier-Rosso, A., Leroy, C., Augustin, P., Delmas, R., Ancellet, G., Athier, G., Bouchou, P., Campistron, B., Cousin, J.-M., Fourmentin, M., and Meyerfeld, Y.: Pic 2005, a field campaign to investigate low-tropospheric ozone variability in the Pyrenees, Atmos. Res., 101, 640–665, https://doi.org/10.1016/j.atmosres.2011.04.014, 2011.

Gomez Kuri, Z.: Analyse des couplages électrodynamiques transitoires à partir d'observations terrestres et spatiales, PhD thesis, University of Toulouse, Toulouse, France, vol. 45, http://www.theses.fr/2021TOU30303 (last access: 17 October 2024), 2021.

Gomez Kuri, Z., Soula, S., Neubert, T., Mlynarczyk, J., and Köhn, C.: Converging Luminosity in Column-Sprite Filaments, Geophys. Res. Lett., 48, e2020GL090364, https://doi.org/10.1029/2020GL090364, 2021.

Gomez-Pelaez, A. J., Ramos, R., Cuevas, E., Gomez-Trueba, V., and Reyes, E.: Atmospheric CO_2, CH_4, and CO with the CRDS technique at the Izaña Global GAW station: instrumental tests, developments, and first measurement results, Atmos. Meas. Tech., 12, 2043–2066, https://doi.org/10.5194/amt-12-2043-2019, 2019.

Gueffier, J.: Régimes de temps et composition atmosphérique associée à la Plateforme Pyrénénne d'Observation de l'Atmosphère : caractérisation par classification hiérarchique de 5 ans de données, PhD thesis, Université Toulouse III, https://theses.fr/2023TOU30385 (last access: 17 October 2024), 2023.

Gueffier, J., Gheusi, F., Lothon, M., Pont, V., Philibert, A., Lohou, F., Derrien, S., Bezombes, Y., Athier, G., Meyerfeld, Y., Vial, A., and Leclerc, E.: Weather regimes and the related atmospheric composition at a Pyrenean observatory characterized by hierarchical clustering of a 5-year data set, Atmos. Chem. Phys., 24, 287–316, https://doi.org/10.5194/acp-24-287-2024, 2024.

Guerova, G., Jones, J., Douša, J., Dick, G., de Haan, S., Pottiaux, E., Bock, O., Pacione, R., Elgered, G., Vedel, H., and Bender, M.: Review of the state of the art and future prospects of the ground-based GNSS meteorology in Europe, Atmos. Meas. Tech., 9, 5385–5406, https://doi.org/10.5194/amt-9-5385-2016, 2016.

Guillaume, B., Liousse, C., Rosset, R., Cachier, H., Van Velthoven, P., Bessagnet, B., and Poisson, N.: ORISAM-TM4: a new global sectional multi-component aerosol model including SOA formation – focus on carbonaceous BC and OC aerosols, Tellus B, 59, 283–302, 2007.

Guillaume, B., Liousse, C., Galy-Lacaux, C., Rosset, R., Gardrat, E., Cachier, H., Bessagnet, B., and Poisson, N.: Modeling exceptional high concentrations of carbonaceous aerosols observed at Pic du Midi in spring–summer 2003: Comparison with Sonnblick and Puy de Dôme, Atmos. Environ., 42, 5140–5149, https://doi.org/10.1016/j.atmosenv.2008.02.024, 2008.

Hadad, D., Baray, J.-L., Montoux, N., Van Baelen, J., Fréville, P., Pichon, J.-M., Bosser, P., Ramonet, M., Yver Kwok, C., Bègue, N., and Duflot, V.: Surface and Tropospheric Water Vapor Variability and Decadal Trends at Two Supersites of CO-PDD (Cézeaux and Puy de Dôme) in Central France, Atmosphere, 9, 302, https://doi.org/10.3390/atmos9080302, 2018.

Haeffelin, M., Barthès, L., Bock, O., Boitel, C., Bony, S., Bouniol, D., Chepfer, H., Chiriaco, M., Cuesta, J., Delanoë, J., Drobinski, P., Dufresne, J.-L., Flamant, C., Grall, M., Hodzic, A., Hourdin, F., Lapouge, F., Lemaître, Y., Mathieu, A., Morille, Y., Naud, C., Noël, V., O'Hirok, W., Pelon, J., Pietras, C., Protat, A., Romand, B., Scialom, G., and Vautard, R.: SIRTA, a ground-based atmospheric observatory for cloud and aerosol research, Ann. Geophys., 23, 253–275, https://doi.org/10.5194/angeo-23-253-2005, 2005.

Hattenberger, G., Verdu, T., Maury, N., Narvor, P., Couvreux, F., Bronz, M., Lacroix, S., Cayez, G., and Roberts, G. C.: Field report: Deployment of a fleet of drones for cloud exploration, Int. J. Micro Air Veh., 14, 17568293211070830, https://doi.org/10.1177/17568293211070830, 2022.

He, W., Jiang, F., Ju, W., Byrne, B., Xiao, J., Nguyen, N. T., Wu, M., Wang, S., Wang, J., Rödenbeck, C., Li, X., Scholze, M., Monteil, G., Wang, H., Zhou, Y., He, Q., and Chen, J. M.: Do State-Of-The-Art Atmospheric CO_2 Inverse Mod-

els Capture Drought Impacts on the European Land Carbon Uptake?, J. Adv. Model. Earth Sy., 15, e2022MS003150, https://doi.org/10.1029/2022MS003150, 2023.

Heiskanen, J., Bruemmer, C., Buchmann, N., Calfapietra, C., Chen, H., Gielen, B., Gkritzalis, T., Hammer, S., Hartman, S., and Herbst, M.: The Integrated Carbon Observation System in Europe, B. Am. Meteorol. Soc., 103, E855–E872, 2022.

Heo, B.-H., Jacoby-Koaly, S., Kim, K.-E., Campistron, B., Bénech, B., and Jung, E.-S.: Use of the Doppler spectral width to improve the estimation of the convective boundary layer height from UHF wind profiler observations, J. Atmos. Ocean. Tech., 20, 408–424, 2003.

Herrmann, E., Weingartner, E., Henne, S., Vuilleumier, L., Bukowiecki, N., Steinbacher, M., Conen, F., Collaud Coen, M., Hammer, E., Jurányi, Z., Baltensperger, U., and Gysel, M.: Analysis of long-term aerosol size distribution data from Jungfraujoch with emphasis on free tropospheric conditions, cloud influence, and air mass transport, J. Geophys. Res.-Atmos., 120, 9459–9480, https://doi.org/10.1002/2015JD023660, 2015.

Hulin, M., Gheusi, F., Lothon, A. M., Pont, V., Lohou, F., Ramonet, M., Delmotte, M., Derrien, S., Athier, G., Meyerfeld, Y., Bezombes, Y., Augustin, P., and Ravetta, F.: Observations of thermally driven circulations in the pyrenees: Comparison of detection methods and impact on atmospheric composition measured at a mountaintop, J. Appl. Meteorol. Clim., 58, 717–740, https://doi.org/10.1175/JAMC-D-17-0268.1, 2019.

Jacoby-Koaly, S.: Application d'un Radar Profileur de Vent UHF à l'Etude de la Couche Limite Atmosphérique, PhD thesis, University of Toulouse, France, https://theses.fr/2000TOU30144 (last access: 17 October 2024), 2000.

Jacoby-Koaly, S., Campistron, B., Bernard, S., Bénech, B., Girard-Ardhuin, F., Dessens, J., Dupont, E., and Carissimo, B.: Turbulent Dissipation Rate In The Boundary Layer Via UHF Wind Profiler Doppler Spectral Width Measurements, Bound.-Lay. Meteorol., 103, 361–389, 2002.

Keeling, C. D., Bacastow, R. B., Bainbridge, A. E., Ekdahl, C. A., Guenther, P. R., Waterman, L. S., and Chin, J. F. S.: Atmospheric carbon dioxide variations at Mauna Loa Observatory, Hawaii, Tellus, 28, 538–551, https://doi.org/10.1111/j.2153-3490.1976.tb00701.x, 1976.

Kim, K.-E., Jung, E.-S., Campistron, B., and Heo, B.-H.: A physical examination of tropopause height and stratospheric air intrusion - A case study, J. Meteorol. Soc. Jpn., Ser. II, 79, 1093–1103, 2001.

Kooijmans, L. J. and Hartogensis, O. K.: Surface-Layer Similarity Functions for Dissipation Rate and Structure Parameters of Temperature and Humidity Based on Eleven Field Experiments, Bound.-Lay. Meteorol., 160, 501–527, 2016.

Kotthaus, S., Haeffelin, M., Drouin, M.-A., Dupont, J.-C., Grimmond, S., Haefele, A., Hervo, M., Poltera, Y., and Wiegner, M.: Tailored Algorithms for the Detection of the Atmospheric Boundary Layer Height from Common Automatic Lidars and Ceilometers (ALC), Remote Sens.-Basel, 12, 3259, https://doi.org/10.3390/rs12193259, 2020.

Lac, C., Chaboureau, J.-P., Masson, V., Pinty, J.-P., Tulet, P., Escobar, J., Leriche, M., Barthe, C., Aouizerats, B., Augros, C., Aumond, P., Auguste, F., Bechtold, P., Berthet, S., Bielli, S., Bosseur, F., Caumont, O., Cohard, J.-M., Colin, J., Couvreux, F., Cuxart, J., Delautier, G., Dauhut, T., Ducrocq, V., Filippi, J.-B., Gazen, D., Geoffroy, O., Gheusi, F., Honnert, R., Lafore, J.-P., Lebeaupin Brossier, C., Libois, Q., Lunet, T., Mari, C., Maric, T., Mascart, P., Mogé, M., Molinié, G., Nuissier, O., Pantillon, F., Peyrillé, P., Pergaud, J., Perraud, E., Pianezze, J., Redelsperger, J.-L., Ricard, D., Richard, E., Riette, S., Rodier, Q., Schoetter, R., Seyfried, L., Stein, J., Suhre, K., Taufour, M., Thouron, O., Turner, S., Verrelle, A., Vié, B., Visentin, F., Vionnet, V., and Wautelet, P.: Overview of the Meso-NH model version 5.4 and its applications, Geosci. Model Dev., 11, 1929–1969, https://doi.org/10.5194/gmd-11-1929-2018, 2018.

Legain, D., Bousquet, O., Douffet, T., Tzanos, D., Moulin, E., Barrie, J., and Renard, J.-B.: High-frequency boundary layer profiling with reusable radiosondes, Atmos. Meas. Tech., 6, 2195–2205, https://doi.org/10.5194/amt-6-2195-2013, 2013.

Leuchner, M., Gubo, S., Schunk, C., Wastl, C., Kirchner, M., Menzel, A., and Plass-Dülmer, C.: Can positive matrix factorization help to understand patterns of organic trace gases at the continental Global Atmosphere Watch site Hohenpeissenberg?, Atmos. Chem. Phys., 15, 1221–1236, https://doi.org/10.5194/acp-15-1221-2015, 2015.

Lohou, F., Lothon, M., Bastin, S., Brut, A., Canut, G., Cheruy, F., Cohard, J.-M., Couvreux, F., Darrozes, J., Dupont, S., Fernandez, R., Jomé, M., Lafont, S., Roehrig, R., Román-Cascón, C., Zouzoua M., and the MOSAI team: Measure and simulate turbulent fluxes over heterogeneous surface: MOSAI, 1st LIAISE Conference (Land surface Interactions with the Atmosphere over the Iberian Semi-arid Environment) and determining evapotranspiration CrossCut Workshop, Lleida, Spain, 27–29 March 2023, https://www.hymex.fr/liaise/LIAISE_conf/Workshop_March_2023/presentations/tuesday/LOHOU_MOSAI_Presentation-GEWEX-LIAISE_202303_vf.pdf (last access: 16 October 2024), 2023.

Lothon, M., Lohou, F., Pino, D., Couvreux, F., Pardyjak, E. R., Reuder, J., Vilà-Guerau de Arellano, J., Durand, P., Hartogensis, O., Legain, D., Augustin, P., Gioli, B., Lenschow, D. H., Faloona, I., Yagüe, C., Alexander, D. C., Angevine, W. M., Bargain, E., Barrié, J., Bazile, E., Bezombes, Y., Blay-Carreras, E., van de Boer, A., Boichard, J. L., Bourdon, A., Butet, A., Campistron, B., de Coster, O., Cuxart, J., Dabas, A., Darbieu, C., Deboudt, K., Delbarre, H., Derrien, S., Flament, P., Fourmentin, M., Garai, A., Gibert, F., Graf, A., Groebner, J., Guichard, F., Jiménez, M. A., Jonassen, M., van den Kroonenberg, A., Magliulo, V., Martin, S., Martinez, D., Mastrorillo, L., Moene, A. F., Molinos, F., Moulin, E., Pietersen, H. P., Piguet, B., Pique, E., Román-Cascón, C., Rufin-Soler, C., Saïd, F., Sastre-Marugán, M., Seity, Y., Steeneveld, G. J., Toscano, P., Traullé, O., Tzanos, D., Wacker, S., Wildmann, N., and Zaldei, A.: The BLLAST field experiment: Boundary-Layer Late Afternoon and Sunset Turbulence, Atmos. Chem. Phys., 14, 10931–10960, https://doi.org/10.5194/acp-14-10931-2014, 2014.

Lothon, M., Barnéoud, P., Gabella, O., Lohou, F., Derrien, S., Rondi, S., Chiriaco, M., Bastin, S., Dupont, J.-C., Haeffelin, M., Badosa, J., Pascal, N., and Montoux, N.: ELIFAN, an algorithm for the estimation of cloud cover from sky imagers, Atmos. Meas. Tech., 12, 5519–5534, https://doi.org/10.5194/amt-12-5519-2019, 2019.

Marenco, A.: Variations of CO and O_3 in the troposphere: evidence of O_3 photochemistry, Atmos. Environ., 20, 911–918, https://doi.org/10.1016/0004-6981(86)90275-1, 1986.

Marenco, A., Gouget, H., Nédélec, P., Pagès, J., and Karcher, F.: Evidence of a long-term increase in tropospheric ozone from Pic du Midi data series – consequences – positive radiative forcing, J. Geophys. Res.-Atmos., 99, 16617–16632, https://doi.org/10.1029/94JD00021, 1994.

Marti, R., Gascoin, S., Houet, T., Ribière, O., Laffly, D., Condom, T., Monnier, S., Schmutz, M., Camerlynck, C., Tihay, J. P., Soubeyroux, J. M., and René, P.: Evolution of Ossoue Glacier (French Pyrenees) since the end of the Little Ice Age, The Cryosphere, 9, 1773–1795, https://doi.org/10.5194/tc-9-1773-2015, 2015.

Maruszczak, N., Sonke, J., Fu, X., and Jiskra, M.: Tropospheric GOM at the Pic du Midi Observatory-Correcting Bias in Denuder Based Observations, Environ. Sci. Technol., 51, 863–869, https://doi.org/10.1021/acs.est.6b04999, 2017.

Mather, J. H. and Voyles, J. W.: The arm climate research facility: A review of structure and capabilities, B. Am. Meteorol. Soc., 94, 377–392, https://doi.org/10.1175/BAMS-D-11-00218.1, 2013.

Maury, N., Roberts, G. C., Couvreux, F., Verdu, T., Narvor, P., Lacroix, S., and Hattenberger, G.: Quantifying the mixing of trade-wind cumulus during the NEPHELAE-EUREC4A field campaign with remotely piloted aircraft, Q. J. Roy. Meteor. Soc., 149, 809–829, https://doi.org/10.1002/qj.4430, 2023.

Milroy, C., Martucci, G., Lolli, S., Loaec, S., Sauvage, L., Xueref-Remy, I., Lavrič, J. V., Ciais, P., Feist, D. G., Biavati, G., and O'Dowd, C. D.: An Assessment of Pseudo-Operational Ground-Based Light Detection and Ranging Sensors to Determine the Boundary-Layer Structure in the Coastal Atmosphere, Adv. Meteorol., 2012, 929080, https://doi.org/10.1155/2012/929080, 2012.

Nadeau, D. F., Pardyjak, E. R., Higgins, C. W., Fernando, H. J. S., and Parlange, M. B.: A simple model for the afternoon and early evening decay of convective turbulence over different land surfaces, Bound.-Lay. Meteorol., 141, 301–324, 2011.

Necki, J., Schmidt, M., Rozanski, K., Zimnoch, M., Korus, A., Lasa, J., Graul, R., and Levin, I.: Six-year record of atmospheric carbon dioxide and methane at a high-altitude mountain site in Poland, Tellus B, 55, 94–104, https://doi.org/10.3402/tellusb.v55i2.16763, 2003.

Neubert, T., Allin, T. H., Stebaek-Nielsen, H., and Blanc, E.: Sprites over Europe, Geophys. Res. Lett., 28, 3585–3588, https://doi.org/10.1029/2001GL013427, 2001.

Neubert, T., Rycroft, M., Farges, T., Blanc, E., Chanrion, O., Arnone, E., Odzimek, A., Arnold, N., Enell, C. F., Turunen, E., Bösinger, T., Mika, Á., Haldoupis, C., Steiner, R. J., van der Velde, O., Soula, S., Berg, P., Boberg, F., Thejll, P., Christiansen, B., Ignaccolo, M., Füllekrug, M., Verronen, P. T., Montanya, J., and Crosby, N.: Recent results from studies of electric discharges in the mesosphere, Surv. Geophys., 29, 71–137, https://doi.org/10.1007/s10712-008-9043-1, 2008.

Nilsson, E., Lohou, F., Lothon, M., Pardyjak, E., Mahrt, L., and Darbieu, C.: Turbulence kinetic energy budget during the afternoon transition – Part 1: Observed surface TKE budget and boundary layer description for 10 intensive observation period days, Atmos. Chem. Phys., 16, 8849–8872, https://doi.org/10.5194/acp-16-8849-2016, 2016a.

Nilsson, E., Lothon, M., Lohou, F., Pardyjak, E., Hartogensis, O., and Darbieu, C.: Turbulence kinetic energy budget during the afternoon transition – Part 2: A simple TKE model, At-

mos. Chem. Phys., 16, 8873–8898, https://doi.org/10.5194/acp-16-8873-2016, 2016b.

Ólafsson, H. and Bougeault, P.: The effect of rotation and surface friction on orographic drag, J. Atmos. Sci., 54, 193–210, https://doi.org/10.1175/1520-0469(1997)054<0193:TEORAS>2.0.CO;2, 1997.

Pandolfi, M., Cusack, M., Alastuey, A., and Querol, X.: Variability of aerosol optical properties in the Western Mediterranean Basin, Atmos. Chem. Phys., 11, 8189–8203, https://doi.org/10.5194/acp-11-8189-2011, 2011.

Pandolfi, M., Ripoll, A., Querol, X., and Alastuey, A.: Climatology of aerosol optical properties and black carbon mass absorption cross section at a remote high-altitude site in the western Mediterranean Basin, Atmos. Chem. Phys., 14, 6443–6460, https://doi.org/10.5194/acp-14-6443-2014, 2014.

Pappalardo, G., Nicolae, D., Makoto, A., Vassilis, A., Balis, D., Behrendt, A., Comeron, A., Gibert, F., Landulfo, E., McCormick, M. P., and Senff, C.: ACTRIS Aerosol, Clouds and Trace Gas Research Infrastructure, EPJ Web Conf., 176, 09004, https://doi.org/10.1051/epjconf/201817609004, 2018.

Philibert, A., Lothon, M., Amestoy, J., Meslin, P.-Y., Derrien, S., Bezombes, Y., Campistron, B., Lohou, F., Vial, A., Canut-Rocafort, G., Reuder, J., and Brooke, J. K.: CALOTRITON: a convective boundary layer height estimation algorithm from ultra-high-frequency (UHF) wind profiler data, Atmos. Meas. Tech., 17, 1679–1701, https://doi.org/10.5194/amt-17-1679-2024, 2024.

Pietersen, H. P., Vilà-Guerau de Arellano, J., Augustin, P., van de Boer, A., de Coster, O., Delbarre, H., Durand, P., Fourmentin, M., Gioli, B., Hartogensis, O., Lohou, F., Lothon, M., Ouwersloot, H. G., Pino, D., and Reuder, J.: Study of a prototypical convective boundary layer observed during BLLAST: contributions by large-scale forcings, Atmos. Chem. Phys., 15, 4241–4257, https://doi.org/10.5194/acp-15-4241-2015, 2015.

Prados-Roman, C., Fernández, M., Gómez-Martín, L., Cuevas, E., Gil-Ojeda, M., Maruszczak, N., Puentedura, O., Sonke, J., and Saiz-Lopez, A.: Atmospheric formaldehyde at El Teide and Pic du Midi remote high-altitude sites, Atmos. Environ., 234, 117618, https://doi.org/10.1016/j.atmosenv.2020.117618, 2020.

Ramonet, M., Ciais, P., Apadula, F., Bartyzel, J., Bastos, A., Bergamaschi, P., Blanc, P. E., Brunner, D., Caracciolo di Torchiarolo, L., Calzolari, F., Chen, H., Chmura, L., Colomb, A., Conil, S., Cristofanelli, P., Cuevas, E., Curcoll, R., Delmotte, M., di Sarra, A., Emmenegger, L., Forster, G., Frumau, A., Gerbig, C., Gheusi, F., Hammer, S., Haszpra, L., Hatakka, J., Hazan, L., Heliasz, M., Henne, S., Hensen, A., Hermansen, O., Keronen, P., Kivi, R., Komínková, K., Kubistin, D., Laurent, O., Laurila, T., Lavric, J. V., Lehner, I., Lehtinen, K. E. J., Leskinen, A., Leuenberger, M., Levin, I., Lindauer, M., Lopez, M., Myhre, C. L., Mammarella, I., Manca, G., Manning, A., Marek, M. V., Marklund, P., Martin, D., Meinhardt, F., Mihalopoulos, N., Mölder, M., Morgui, J. A., Necki, J., O'Doherty, S., O'Dowd, C., Ottosson, M., Philippon, C., Piacentino, S., Pichon, J. M., Plass-Duelmer, C., Resovsky, A., Rivier, L., Rodó, X., Sha, M. K., Scheeren, H. A., Sferlazzo, D., Spain, T. G., Stanley, K. M., Steinbacher, M., Trisolino, P., Vermeulen, A., Vítková, G., Weyrauch, D., Xueref-Remy, I., Yala, K., and Yver Kwok, C.: The fingerprint of the summer 2018 drought in Europe on ground-based atmospheric

CO$_2$ measurements, Philos. T. Roy. Soc. B, 375, 20190513, https://doi.org/10.1098/rstb.2019.0513, 2020.

RESIF: RESIF-RENAG French national Geodetic Network, https://doi.org/10.15778/resif.rg, 2017.

Reuder, J., Båserud, L., Jonassen, M. O., Kral, S. T., and Müller, M.: Exploring the potential of the RPA system SUMO for multipurpose boundary-layer missions during the BLLAST campaign, Atmos. Meas. Tech., 9, 2675–2688, https://doi.org/10.5194/amt-9-2675-20168, 2016.

Román-Cascón, C., Yagüe, C., Mahrt, L., Sastre, M., Steeneveld, G.-J., Pardyjak, E., van de Boer, A., and Hartogensis, O.: Interactions among drainage flows, gravity waves and turbulence: a BLLAST case study, Atmos. Chem. Phys., 15, 9031–9047, https://doi.org/10.5194/acp-15-9031-2015, 2015.

Román-Cascón, C., Yagüe, C., Arrillaga, J. A., Lothon, M., Pardyjak, E. R., Lohou, F., Inclán, R. M., Sastre, M., Maqueda, G., Derrien, S., Meyerfeld, Y., Hang, C., Campargue-Rodríguez, P., and Turki, I.: Comparing mountain breezes and their impacts on CO$_2$ mixing ratios at three contrasting areas, Atmos. Res., 221, 111–126, https://doi.org/10.1016/j.atmosres.2019.01.019, 2019.

Rotach, M. W., Wohlfahrt, G., Hansel, A., Reif, M., Wagner, J., and Gohm, A.: The World is Not Flat: Implications for the Global Carbon Balance, B. Am. Meteorol. Soc., 95, 1021–1028, https://doi.org/10.1175/BAMS-D-13-00109.1, 2014.

Roudier, T., Maiherbe, J.-M., Rozelot, J.-P., Mein, P., and Muller, R.: Five decades of solar research at the Pic du Midi Turret-Dome (1960–2010). Part I: Overview of instrumentation and observations, Journal of Astronomical History and Heritage, 24, 585–606, 2021.

Saiz-Lopez, A., Sitkiewicz, S., Roca-Sanjuán, D., Oliva-Enrich, J., Dávalos, J., Notario, R., Jiskra, M., Xu, Y., Wang, F., Thackray, C., Sunderland, E., Jacob, D., Travnikov, O., Cuevas, C., Acuña, A., Rivero, D., Plane, J., Kinnison, D., and Sonke, J.: Photoreduction of gaseous oxidized mercury changes global atmospheric mercury speciation, transport and deposition, Nature Communications, 9, 4796, https://doi.org/10.1038/s41467-018-07075-3, 2018.

Saunois, M., Stavert, A. R., Poulter, B., Bousquet, P., Canadell, J. G., Jackson, R. B., Raymond, P. A., Dlugokencky, E. J., Houweling, S., Patra, P. K., Ciais, P., Arora, V. K., Bastviken, D., Bergamaschi, P., Blake, D. R., Brailsford, G., Bruhwiler, L., Carlson, K. M., Carrol, M., Castaldi, S., Chandra, N., Crevoisier, C., Crill, P. M., Covey, K., Curry, C. L., Etiope, G., Frankenberg, C., Gedney, N., Hegglin, M. I., Höglund-Isaksson, L., Hugelius, G., Ishizawa, M., Ito, A., Janssens-Maenhout, G., Jensen, K. M., Joos, F., Kleinen, T., Krummel, P. B., Langenfelds, R. L., Laruelle, G. G., Liu, L., Machida, T., Maksyutov, S., McDonald, K. C., McNorton, J., Miller, P. A., Melton, J. R., Morino, I., Müller, J., Murguia-Flores, F., Naik, V., Niwa, Y., Noce, S., O'Doherty, S., Parker, R. J., Peng, C., Peng, S., Peters, G. P., Prigent, C., Prinn, R., Ramonet, M., Regnier, P., Riley, W. J., Rosentreter, J. A., Segers, A., Simpson, I. J., Shi, H., Smith, S. J., Steele, L. P., Thornton, B. F., Tian, H., Tohjima, Y., Tubiello, F. N., Tsuruta, A., Viovy, N., Voulgarakis, A., Weber, T. S., van Weele, M., van der Werf, G. R., Weiss, R. F., Worthy, D., Wunch, D., Yin, Y., Yoshida, Y., Zhang, W., Zhang, Z., Zhao, Y., Zheng, B., Zhu, Q., Zhu, Q., and Zhuang, Q.: The Global Methane Budget 2000–2017, Earth Syst. Sci. Data, 12, 1561–1623, https://doi.org/10.5194/essd-12-1561-2020, 2020.

Scorer, R. S.: Theory of airflow over moutains. Part IV: Separation of flow from the surface, Q. J. Roy. Meteor. Soc., 81, 340–350, 1955.

Seity, Y., Brousseau, P., Malardel, S., Hello, G., Bénard, P., Bouttier, F., Lac, C., and Masson, V.: The AROME-France Convective-Scale Operational Model, Mon. Weather Rev., 139, 976–991, https://doi.org/10.1175/2010MWR3425.1, 2011.

Smith, R. B.: On severe downslope winds, J. Atmos. Sci., 42, 2597–2603, https://doi.org/10.1175/1520-0469(1985)042<2597:OSDW>2.0.CO;2, 1985.

Soula, S., Defer, E., Füllekrug, M., van der Velde, O., Montanyà, J., Bousquet, O., Mlynarczyk, J., Coquillat, S., Pinty, J.-P., Rison, W., Krehbiel, P., Thomas, R., and Pedeboy, S.: Time and space correlation between sprites and their parent lightning flashes for a thunderstorm observed during the HyMeX campaign, J. Geophys. Res.-Atmos., 120, 11552–11574, https://doi.org/10.1002/2015JD023894, 2015.

Soula, S., Mlynarczyk, J., Füllekrug, M., Pineda, N., Georgis, J. F., van der Velde, O., Montanyà, J., and Fabró, F.: Dancingsprites: Detailed analysis of two case studies, J. Geophys. Res., 122, 3173–3192, https://doi.org/10.1002/2016JD025548, 2017.

Steinacker, R.: Area-height distribution and its relation to the valley wind, Beitr. Phys. Atmos., 57, 64–71, 1984.

Stevens, B., Farrell, D., Hirsch, L., Jansen, F., Nuijens, L., Serikov, I., Brügmann, B., Forde, M., Linne, H., Lonitz, K., and Prospero, J. M.: The Barbados cloud observatory: Anchoring investigations of clouds and circulation on the edge of the itcz, B. Am. Meteorol. Soc., 97, 735–754, https://doi.org/10.1175/BAMS-D-14-00247.1, 2016.

Suess, E., Aemisegger, F., Sonke, J., Sprenger, M., Wernli, H., and Winkel, L.: Marine versus Continental Sources of Iodine and Selenium in Rainfall at Two European High-Altitude Locations, Environ. Sci. Technol., 53, 1905–1917, https://doi.org/10.1021/acs.est.8b05533, 2019.

Sun, J., Hermann, M., Yuan, Y., Birmili, W., Collaud Coen, M., Weinhold, K., Madueño, L., Poulain, L., Tuch, T., Ries, L., Sohmer, R., Couret, C., Frank, G., Brem, B. T., Gysel-Beer, M., Ma, N., and Wiedensohler, A.: Long-term trends of black carbon and particle number concentration in the lower free troposphere in Central Europe, Environmental Sciences Europe, 33, 47, https://doi.org/10.1186/s12302-021-00488-w, 2021.

Szénási, B., Berchet, A., Broquet, G., Segers, A., van der Gon, H. D., Krol, M., Hullegie, J. J. S., Kiesow, A., Günther, D., Petrescu, A. M. R., Saunois, M., Bousquet, P., and Pison, I.: A pragmatic protocol for characterising errors in atmospheric inversions of methane emissions over Europe, Tellus B, 73, 1–23, 2021.

Tenkanen, M., Tsuruta, A., Rautiainen, K., Kangasaho, V., Ellul, R., and Aalto, T.: Utilizing Earth Observations of Soil Freeze/Thaw Data and Atmospheric Concentrations to Estimate Cold Season Methane Emissions in the Northern High Latitudes, Remote Sens.-Basel, 13, 5059, https://doi.org/10.3390/rs13245059, 2021.

Thompson, R. L., Broquet, G., Gerbig, C., Koch, T., Lang, M., Monteil, G., Munassar, S., Nickless, A., Scholze, M., Ramonet, M., Karstens, U., van Schaik, E., Wu, Z., and Rödenbeck, C.: Changes in net ecosystem exchange over Europe during the 2018 drought based on atmospheric observations, Philos. T. Roy. Soc. B, 375, 20190512, https://doi.org/10.1098/rstb.2019.0512, 2020.

Thompson, R. L., Groot Zwaaftink, C. D., Brunner, D., Tsuruta, A., Aalto, T., Raivonen, M., Crippa, M., Solazzo, E., Guizzardi, D., Regnier, P., and Maisonnier, M.: Effects of extreme meteorological conditions in 2018 on European methane emissions estimated using atmospheric inversions, Philos. T. Roy. Soc. A, 380, 20200443, https://doi.org/10.1098/rsta.2020.0443, 2021.

Tinorua, S., Denjean, C., Nabat, P., Bourrianne, T., Pont, V., Gheusi, F., and Leclerc, E.: Higher absorption enhancement of black carbon in summer shown by 2-year measurements at the high-altitude mountain site of Pic du Midi Observatory in the French Pyrenees, Atmos. Chem. Phys., 24, 1801–1824, https://doi.org/10.5194/acp-24-1801-2024, 2024.

Tomicic, M., Soula, S., Defer, E., Prieur, S., Mlynarczyk, J., and Farges, T.: Dancing sprites above a Lightning Mapping Array – An analysis of the storm and flash/sprite developments, J. Geophys. Res. Atmos., 126, D035059, https://doi.org/10.1029/2021JD035059, 2021.

Tsamalis, C., Ravetta, F., Gheusi, F., Delbarre, H., and Augustin, P.: Mixing of free-tropospheric air with the lowland boundary layer during anabatic transport to a high altitude station, Atmos. Res., 143, 425–437, https://doi.org/10.1016/j.atmosres.2014.03.011, 2014.

Tsikerdekis, A., Zanis, P., Steiner, A. L., Solmon, F., Amiridis, V., Marinou, E., Katragkou, E., Karacostas, T., and Foret, G.: Impact of dust size parameterizations on aerosol burden and radiative forcing in RegCM4, Atmos. Chem. Phys., 17, 769–791, https://doi.org/10.5194/acp-17-769-2017, 2017.

Whiteman, C. D.: Observations of Thermally Developed Wind Systems in Mountainous Terrain, in: Atmospheric Processes Over Complex Terrain, edited by: Blumen, W., Meteorological Monographs, 23, no. 45, American Meteorological Society, Boston, Massachusetts, Chap. 2, 5–42, https://doi.org/10.1007/978-1-935704-25-6_2, 1990.

Whittlestone, S. and Zahorowski, W.: Baseline radon detectors for shipboard use: Development and deployment in the First Aerosol Characterization Experiment (ACE 1), J. Geophys. Res.-Atmos., 103, 16743–16751, https://doi.org/10.1029/98JD00687, 1998.

Yang, X., Jiskra, M., and Sonke, J.: Experimental rainwater divalent mercury speciation and photoreduction rates in the presence of halides and organic carbon, Sci. Total Environ., 697, 133821, https://doi.org/10.1016/j.scitotenv.2019.133821, 2019.

Yver Kwok, C., Laurent, O., Guemri, A., Philippon, C., Wastine, B., Rella, C. W., Vuillemin, C., Truong, F., Delmotte, M., Kazan, V., Darding, M., Lebègue, B., Kaiser, C., Xueref-Rémy, I., and Ramonet, M.: Comprehensive laboratory and field testing of cavity ring-down spectroscopy analyzers measuring H_2O, CO_2, CH_4 and CO, Atmos. Meas. Tech., 8, 3867–3892, https://doi.org/10.5194/amt-8-3867-2015, 2015.

Zouzoua, M., Bastin, S., Chiriaco, M., Lohou, F., Lothon, M., Jome, M., Mallet, C., Barthes, L., and Canut, G.: Using a data-driven statistical model to better evaluate surface turbulent heat fluxes in weather and climate numerical models: a demonstration study, EGUsphere [preprint], https://doi.org/10.5194/egusphere-2024-568, 2024.